Summary of the results obtained during the project „Smart tripodal ligands" (OTKA K101541)

1. Introduction

The metal binding side chains in metalloproteins are generally far away from each other in the primary sequences, and they are often separated by more than a hundred amino acids. Sequences within the polypeptide chains generally have well-defined conformations due to the tertiary structure of the proteins, which provides a preorganized binding site for the metal ion(s) in metalloproteins. Linear peptides have long since been used to mimic the metal binding sites of metalloproteins and metalloenzymes. However, oligopeptides are generally flexible ligands, and the absence preorganized structure obviously reduces the analogy with the metalloproteins. In order to develop efficient structural/functional models of metalloproteins based on peptide-like ligands, three basic options are possible: (i) short linear peptides with high 'density' of metal binding side-chains, (ii) cyclic or (iii) tripodal peptides, which have even more favourable spatial distribution of the donor sites. During our work, we tried to examine all these possibilities, focussing on (i) and (iii). To this end, we studied some linear or cyclic peptides copying the consensus catalytic metal binding site of matrix metalloproteinase 13 ($\mathbf{L^1}$), the putative metal binding sequences of ZnT3 zinc transporter ($\mathbf{L^2}$-$\mathbf{L^4}$), as well as some His-rich tripodal peptides containing both N- and C-terminal histidines ($\mathbf{L^5}$-$\mathbf{L^8}$, see Figure 1).

L^1: ***Ac*-Lys-Ala-His-Glu-Phe-Gly-His-Ser-Leu-Gly-Leu-Asp-His-Ser-Lys-*NH_2***

L^2: ***Ac*-Arg-His-Gln-Ala-Gly-Pro-Pro-His-Ser-His-Arg-*NH_2***

L^4: ***Ac*-Pro-Phe-His-His-Cys-His-Arg-Asp-*NH_2***

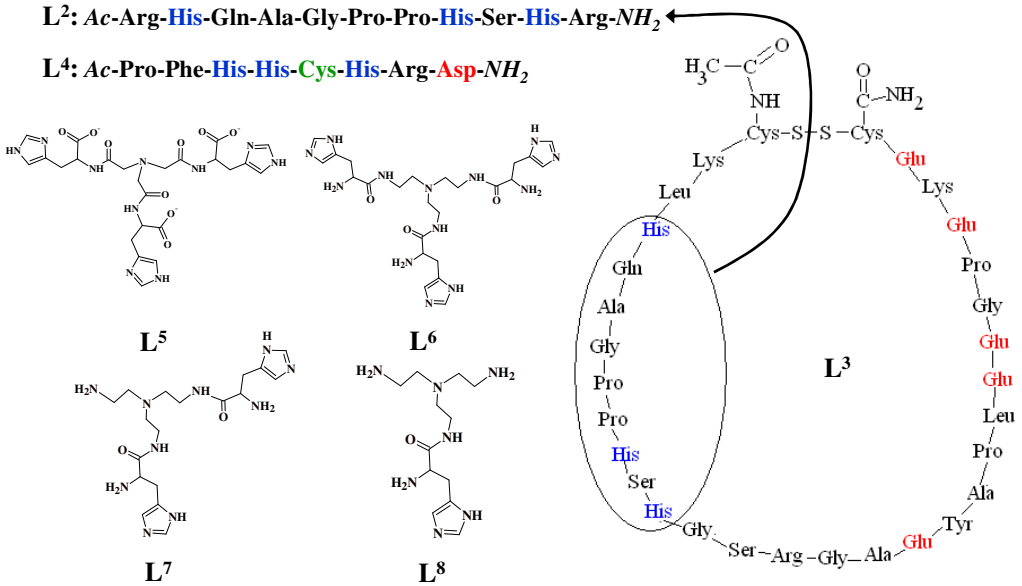

Figure 1. Schematic structures of the studied peptide ligands

The favourable and preorganized spatial distribution of donor atoms in tripodal ligands has been long time recognised and applied to develop metal ion chelators for a variety of purposes, such as metal ion sequestering agents, structural/functional models of metalloproteins or to develop supramolecular assemblies. The majority of these studies deal with tri- or tetradentate tripodal ligands, such as tris-(2-aminoethyl)amine (tren), nitrilotriacetic acid (nta), or *cis,cis*-1,3,5-triaminocyclohexane (tach). During our work we prepared N-substituted derivatives of tach and tren (Figure 2). Such modifications may provide additional donor site(s), may influence the steric environment around the metal centre or may help to introduce further metal binding site(s) in order to create polynuclear

complexes. All ligands, except $\mathbf{L}^{9a-d}$, have been synthesized by us, which caused a number of unexpected difficulties (especially in the cases of $\mathbf{L}^{5-8}$ and $\mathbf{L}^{13/18}$), which, unfortunately, significantly impeded the progress of the work. The tripodal ligand $\mathbf{L}^{9a}$ and its derivatives have been synthesized by our cooperating partners at the University of Turku.

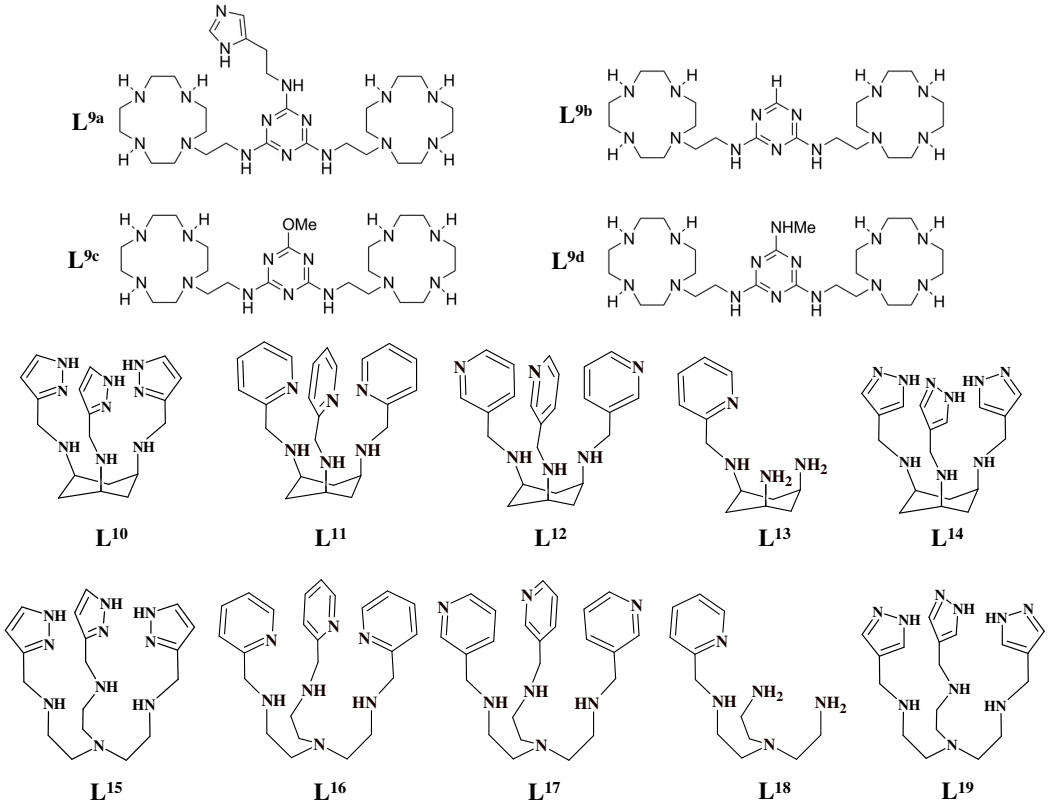

Figure 2. Schematic structures of the studied non-peptide ligands

Among the ligands listed in Figures 1 and 2 only $\mathbf{L}^{11}$ and $\mathbf{L}^{16}$ have been reported earlier, but these studies are restricted to copper(II) and zinc(II), and no thermodynamic data on the metal complexes of $\mathbf{L}^{11}$ is reported in the literature.

2. Results

2.1 A minimalist chemical model of matrix metalloproteinases - can small peptides mimic the more rigid metal binding sites of proteins? (copper(II) and zinc(II) complexes of $\mathbf{L}^{1}$, [1])

In order to mimic the active centre of matrix metalloproteinases (MMPs), we synthesized a pentadecapeptide $\mathbf{L}^{1}$ corresponding to the catalytic zinc(II) binding site of human MMP-13. The multi-domain structural organization of MMPs fundamentally determines their metal binding affinity, catalytic activity and selectivity. Our potentiometric, UV-visible, CD, EPR, NMR, mass spectrometric and kinetic studies are aimed to explore the usefulness of such flexible peptides to mimic the more preorganized metal binding sites of proteins, to examine the intrinsic metal binding properties of this naked sequence, as well as to contribute to the development of a minimalist, peptide-based chemical model of MMPs, including the catalytic properties. Since the multiimidazole environment is also characteristic for copper(II), and recently copper(II) containing variants of MMPs have been identified, we also studied the copper(II) complexes of the above peptide.

Around pH 6-7 the peptide, similarly to the active sites of MMPs, offers a $\{3N_{im}\}$ binding site for both zinc(II) and copper(II), *i.e.* $\mathbf{L^1}$ behaves as a tridentate ligand through the formation of macrochelates. Since this model peptide is virtually unstructured in aqueous solution, its zinc(II) and copper(II) binding affinity is rather modest in comparison with the apo-enzymes (the log K value for the reaction $M(II) + H_2\mathbf{L^1} = MH_2\mathbf{L^1}$ are log K = 4.46 and 7.77 for Zn(II) and Cu(II), respectively). Nevertheless, this flexible peptide is able to mimic any other basic features of the MMP active sites: the main species around pH 7 ($ZnH_2\mathbf{L^1}$, in which two lysine side-chains are protonated) possesses a $\{3N_{im},H_2O\}$ coordination environment, the deprotonation of the zinc-bound water takes place near to the physiological pH, the species formed in this way, $ZnH_2\mathbf{L^1}(OH)$ and $ZnH_2\mathbf{L^1}(OH)_2$, have notable hydrolytic activity between pH 7-9. Since hydroxamic acids are well-known inhibitors of MMP, we also studied interaction of the zinc(II) complexes with benzohydroxamic acid (Bh). The complex $ZnH_2\mathbf{L^1}$ forms relatively stable ternary complexes with Bh (log K ($ZnH_2\mathbf{L^1}$+Bh = $Zn(H_2\mathbf{L^1})Bh$) = 4.55).

In the case of copper(II), the formation of amide coordinated species above pH 7 abolished the analogy with the copper(II) containing MMP variant. According to our potentiometric, EPR and MS study, the pentadecapeptide $\mathbf{L^1}$ forms both dinuclear and trinuclear complexes with copper(II). According to the presence of three, well separated His-subunits, which act as anchoring groups for the amide-NH deprotonations, each copper(II) ions have $\{N_{im},2N^-\}/\{N_{im},3N^-\}$ coordination environment, depending on the pH. All oligonuclear complexes have detectable, but unresolved EPR spectra, indicating weakly interacting metal ions, as expected based on the well separated His units within the peptide chain.

2.2 A comparative study on the possible zinc binding sites of the human ZnT3 zinc transporter protein (Ni(II), Cu(II) and Zn(II) complexes of $\mathbf{L^{2-4}}$, [2])

Dysfunction of zinc homeostasis was found to be associated with several chronic diseases, e.g. asthma, diabetes and neurodegenerative disorders, which explains the increasing interest in zinc transporter proteins. ZnT3, which is a brain specific zinc transporter protein located in the membranes of zinc-rich glutamatergic presynaptic vesicles, and is responsible for most zinc released into the synaptic space. Although synaptic zinc is believed to act as an intracellular signaling factor and a neuromodulator, it was also shown that high zinc concentrations triggers the aggregation of β-amyloid, and thus can be related to the amyloid neuropathology of Alzheimer's disease. Despite the above-mentioned importance of Zn(II) in neuronal physiology, the mechanism of zinc translocation and the metal binding site(s) of ZnT3 and other ZnT proteins are only poorly understood, since a three-dimensional structure is not available. An intriguing feature shared by most ZnT proteins is an intracellular His-rich loop between the transmembrane domains IV–V. The His-rich loop as a putative metal binding site of ZnT proteins is widely accepted in the literature, and its role in zinc sequestration, membrane transport and/or its regulation is generally assumed. However, the loops between the transmembrane domains IV–V of human ZnT1, ZnT3, ZnT5, ZnT6, ZnT7 and ZnT10 proteins contain 10, 3, 15, 1, 20 and 0 His residues, respectively, suggesting that zinc sequestering and sensing (and transport) mechanisms of ZnTs may differ from each other, and thus may involve other metal binding sites, too. Indeed, a recent phylogenetic analysis of the Cation Diffusion Facilitator family indicated that the well conserved N-terminal HHCH sequence may also be involved in zinc binding.

In order to analyze the metal binding ability of hZnT3 protein, we studied the zinc(II) complexes of three peptides mimicking the above-mentioned possible metal binding sequences. The peptide $\mathbf{L^2}$ is a minimalist and the cyclic peptide $\mathbf{L^3}$ is a complete model of the

intracellular His-rich loop of ZnT3. Finally $\mathbf{L^4}$ is a copy of the conserved cytoplasmic N-terminal metal binding motif of human ZnT3. As recently reported, the bacterial zinc transporter YiiP may exploits tetrahedral coordination geometry to select for zinc(II) against other transition metal ions that prefer octahedral coordination. In order to study the possibility of similar, geometry-based metal ion selectivity of these putative metal binding sites, the interaction of the above-mentioned peptides with nickel(II) and copper(II) – having a strong preference for (distorted) octahedral geometry – was also investigated.

In the physiological pH-range, the $\mathbf{ZnL^2}$, $\mathbf{ZnH_3L^3}$ and $\mathbf{ZnL^4}$ complexes are the major species in the corresponding binary systems, with $\{3N_{im}\}$, $\{3N_{im},2/3O_{amide}\}$ and $\{3N_{im},S^-\}$ coordination environments, respectively. Among the three peptides only $\mathbf{L^4}$ provides a real high affinity binding site to zinc, which can be well demonstrated by calculating the apparent (conditional) dissociation constant ($K_D = (\Sigma[MH_xL]/([M^{2+}]_{free} \times (\Sigma[H_xL]_{free})$ at pH 7.4 and a 1 : 1 metal-to-ligand ratio: $K_D = 3.0 \times 10^{-8}$ M ($\mathbf{L^4}$), $K_D = 1.4 \times 10^{-6}$ M ($\mathbf{L^3}$), $K_D = 8 \times 10^{-4}$ M ($\mathbf{L^2}$). Although the direct comparison of these values with those determined for zinc transporter proteins is probably misleading, $\mathbf{L^4}$ has nearly the same zinc binding affinity as *e.g.* the zinc transporter YiiP ($K_D = 1.7 \times 10^{-6}$ M). The preference of zinc(II) for $\mathbf{L^4}$ between pH 5 and 10, among the three peptides, can be also shown by the predominance curves (competition plots) for a solution containing equimolar concentrations of $\mathbf{L^2}$, $\mathbf{L^3}$, $\mathbf{L^4}$ and zinc(II) (Figure 3).

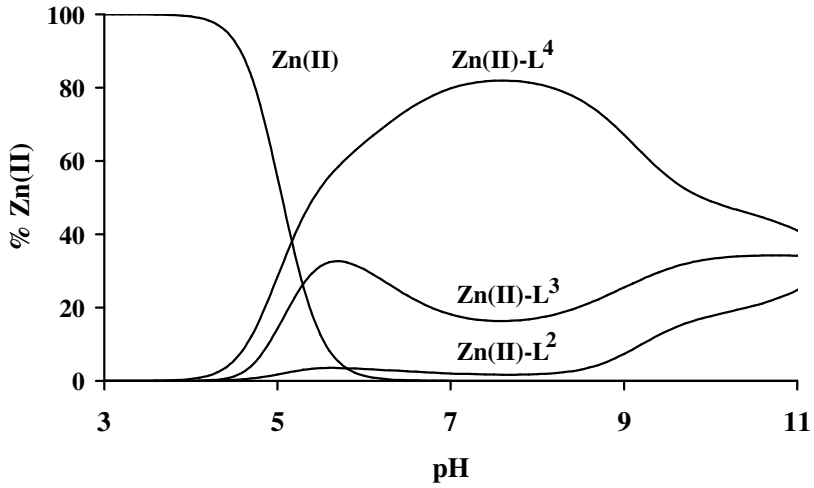

Figure 3. Calculated competition plot between the zinc(II) complexes of $\mathbf{L^2}$, $\mathbf{L^3}$ and $\mathbf{L^4}$ ($[\mathbf{L^2}]=[\mathbf{L^2}]=[\mathbf{L^2}] = [Zn^{2+}] = 0.001$ M).

Although the minimalist ($\mathbf{L^2}$) and the more complete ($\mathbf{L^3}$) models of the His-rich loop contain identical primary donor sites, the latter binds more strongly to zinc(II) as a consequence of its preorganized structure, which provides additional amide oxygen coordination besides the three imidazole rings. A comparison of $\mathbf{L^2}$ and $\mathbf{L^3}$ peptides also shows that by the use of the minimalist model of metal binding sites one may underestimate the sequestering properties. In addition, neither $\mathbf{L^2}$ nor $\mathbf{L^3}$ possesses notable selectivity towards zinc(II) in comparison with nickel(II). However, the N-terminal sequence ($\mathbf{L^4}$) shows a highly preferred coordination to zinc(II) between pH 5 and 8 (Figure 4), although the nickel(II) complexes become dominant above pH 8.5 due to the formation of amide coordinated complexes. This preference for zinc(II) is probably due to the tetrahedral arrangement of the adjacent thiolate and imidazole donors in $\mathbf{L^4}$, which is less favourable for the octahedral nickel(II). The high zinc binding affnity and selectivity of $\mathbf{L^4}$ in the neutral pH-range indicates that zinc(II) binding to the N-terminal tail of human ZnT3 may be involved in its biological activity.

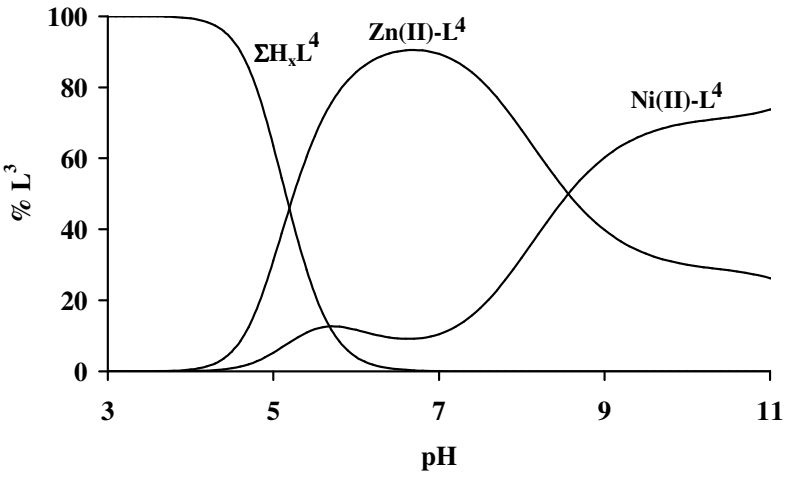

Figure 4. Calculated competition plot between nickel(II) and zinc(II) complexes of $\mathbf{L^4}$ ($[\mathbf{L^4}] = [Zn^{2+}] = [Ni^{2+}] = 0.001$ M)

2.3 Tuning the coordination properties of multi-histidine peptides by using a tripodal scaffold: solution chemical study and catechol oxidase mimicking (copper(II) complexes of $\mathbf{L^5}$ and $\mathbf{L^6}$, [3])

As the study described in ***2.1*** and ***2.2*** indicated, in linear multi-His peptides the side-chain donors have relatively low metal binding ability in the physiological pH range as compared to the proteins, mainly due to the lack of pre-organized (tertiary) structure. To avoid this difficulty, preorganized ligands with more favourable spatial distribution of the donor sites should be used. Recently, a cyclic His-rich decapeptide has been shown to be an efficient scaffold for highly stable multiimidazole coordination. Tripodal peptidomimetics are also suitable for this purpose. These ligands have several advantages in addition to the pre-organized structure and enhanced chelate effect. Using different amino acids, it is relatively easy to fine-tune the metal ion binding ability. Adequate substitution of the tripodal platform may influence the electronic structure and steric environment of the metal centres and may ensure the formation of oligonuclear complexes with relatively short metal-metal separation, which would allow the cooperation of metal centres during the catalytic processes.
Our aim was to take advantage of the preorganized structure of tripodal scaffolds and the metal binding ability of histidine units in order to develop new oligometallic copper(II) cores, which may potentially mimic the function of oxidase enzymes. Although a number of reports has been published on the SOD mimicking properties of copper(II)-peptide complexes, only a few can be found on their oxidase activity. For example, we and others also reported earlier that copper(II) complexes of linear multihistidine peptides may possess (rather modest) cathecol oxidase mimicking properties. During our work, we synthesized two new histidine derivatives based on nta and tren as tripodal platforms ($\mathbf{L^5}$ and $\mathbf{L^6}$), which contain C- and N-terminal histidines, respectively, and studied the solution equilibrium and spectroscopic properties of their copper(II) complexes. To screen the oxidase mimetic properties of these complexes, their catecholase activity was also studied by using 3,5-di-*tert*-butylcatechol (H_2DTBC) as model substrate.

At 1:1 metal-to-ligand ratio and between pH 5-9 the two ligands behave as the corresponding dipeptides containing N/C-terminal histidine. The multiimidazole environment present below pH 5 in $CuH_3\mathbf{L^6}$/$CuH_2\mathbf{L^6}$ switches to *bis*-histamine-like coordination in $CuH\mathbf{L^6}$/$Cu\mathbf{L^6}$, while at higher pH the participation of the tertiary amine in the fused chelate rings results in a unique $\{N_{im},N^-,N_{tert},N^-\}$ binding mode in $CuH_{-2}\mathbf{L^6}$. It means that above pH 5

only one free (loosely bound) N-terminal histidine leg is available for binding a further metal ion, which results in the formation of oligonuclear complexes with 3:2 metal-to-ligand ratio. Since the metal ion environment in the corresponding mono- and trinuclear complexes (*e.g.* in Cu$\mathbf{L^6}$ and $Cu_3\mathbf{L^6}_2$) are nearly identical, trinuclear complexes are present even at 1/1 metal-to-ligand ratio. On the other hand, the Gly-His-like $\{N_{tert},N^-,N_{im},O\}$ coordination in $CuH_x\mathbf{L^5}$ (x = 2, 1, 0, -1) leaves two unbound C-terminal histidine legs, which provides the possibility for the formation of dinuclear species with 2:1 metal-to-ligand ratio. Consequently, the two metal binding sites of $\mathbf{L^5}$ are distinctly different (*e.g.* $\{N_{tert},N^-,N_{im},O; 2N^-,2N_{im}\}$ in $Cu_2H_{-3}\mathbf{L^5}$), and due to the outstanding stability of Gly-His-like coordination dinuclear complexes are formed only at metal ion excess.

The copper(II) complexes of the two ligands have different oxidase mimetic properties, too. Under the optimal conditions used for $\mathbf{L^6}$ (pH 7.8, Cu(II)/$\mathbf{L^6}$ = 3/2) trinuclear complexes (mostly $Cu_3H_{-1}\mathbf{L^6}_2$) are the pre-active species. Nevertheless, oxidation of H_2DTBC proceeds in a one-electron transfer pathway, with the participation of a single Cu^{2+} center; the other metal ions might only have inferior contribution in substrate binding. In this system the copper(II)-catecholate/copper(I)-semiquinone valence tautomerism is shifted towards the copper(II)-catecholate form. One of these tautomers reacts with dioxygen in the rate determining step, resulting the formation of oxygenated radical intermediate(s). After a subsequent intramolecular electron transfer DTBQ and H_2O_2 molecules are released, regenerating the copper(II) centre and allowing the coordination of a new substrate (Scheme 1).

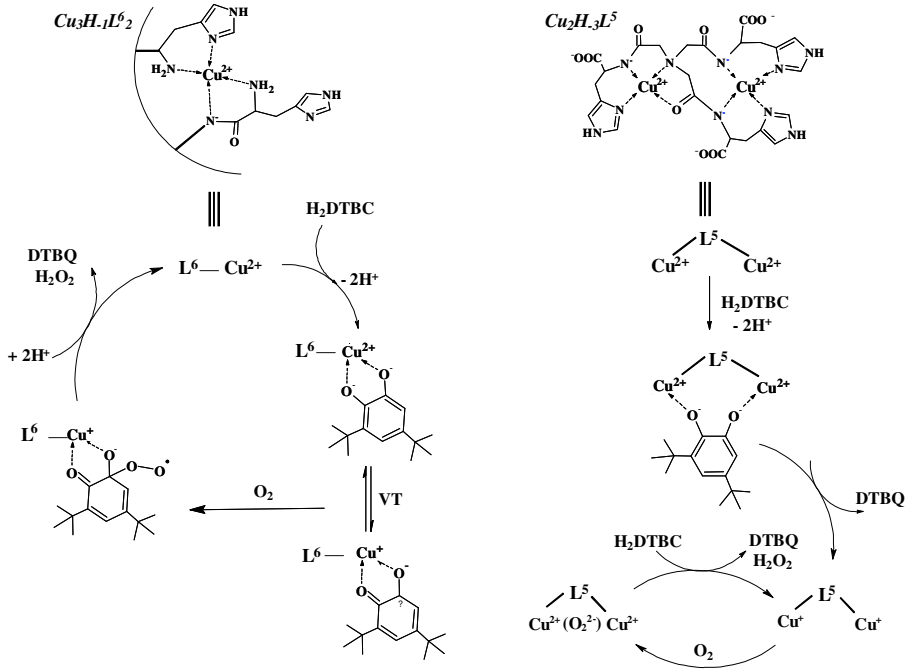

Scheme 1. Proposed mechanism of catalytic oxidation of 3,5-di-*tert*-butylcatechol by copper(II) complexes of $\mathbf{L^5}$ and $\mathbf{L^6}$ ligands.

In contrast, the oxidation in the Cu(II)-$\mathbf{L^5}$-H_2DTBC system is catalyzed by two co-operating copper(II) centres, similarly to the catecholase enzymes. Even though dicopper(II) species are formed already at pH 4 in Cu(II)-$\mathbf{L^5}$ 2:1 system, the tendency of catecholase-like activity follows the formation of $Cu_2H_{-3}\mathbf{L^5}$. After coordination of the substrate to the dicopper(II) core, DTBQ and dicopper(I) species are formed in a fast electron transfer process. The reduced metal centres are re-oxidized by dioxygen, yielding probably a Cu(II)-O_2^{2-}-Cu(II) species, as it is often proposed. This in turn reacts with an incoming second

substrate molecule, and the dicopper(I) species is regenerated after releasing the second DTBQ and H_2O_2 (via proton transfer).

Since hydrogen peroxide does not seem to be produced in stoichiometric quantity in either catalytic system, the participation of H_2O_2 in the catalytic reaction can be suggested. Most probably, as a widely known oxidizing agent, the peroxide molecule might contribute to the reoxidation of Cu(I) centre(s) to Cu(II), as it was previously described for other catalytic copper(II) complexes.

It is interesting to note, that in case of both ligands amide coordinated complexes are the pre-active species during H_2DTBC oxidation. Although the reactivity of catecholates increases considerably with increasing pH, the thermodynamic stability of amide coordinated complexes also increases, thus the +2 oxidation state of copper becomes more stabilized. Therefore, we hypothesize that the deprotonated amides may facilitate the coordination of catechols by abstracting protons (re-protonation), which opens the possibility for the formation of copper(I) complexes.

2.4 Modulating the coordination chemistry of the tripodal platform tris(2-aminoethyl)amine (tren) by gradual N-substitution with L-histidyl units (zinc(II) complexes of $\mathbf{L^6}$, $\mathbf{L^7}$ and $\mathbf{L^8}$, [4])

Only a few reports are available in the literature describing metal ion interactions with tripodal peptides, and most of them are related to sulphur-containing ligands (Cys or Met derivatives). The high donor group 'density' of non-protected histidines attached to the tripodal platform tren provides the formation of highly stable mono- and oligonuclear complexes (see for example part ***2.3***). In order to explore this possibility, we prepared $\mathbf{L^7}$ and $\mathbf{L^8}$ (beside $\mathbf{L^6}$). Our aim was to establish the effect of gradual N-histidyl substitution on the coordination chemical properties. To this end we performed pH potentiometric, NMR and Maldi-TOF MS studies to determine the solution equilibrium and structural properties of the zinc(II) complexes formed in presence of $\mathbf{L^6}$, $\mathbf{L^7}$ and $\mathbf{L^8}$.

In the zinc(II)-$\mathbf{L^8}$ system four differently protonated species could be identified by potentiometry (Figure 5). Parallel with the formation of $ZnH_2\mathbf{L^8}$ the ^{1}H NMR signals of the imidazole, αCH and βCH_2 groups significantly broaden, which together with the equilibrium data indicates histamine-type {N_{im},NH_2} binding mode in $ZnH_2\mathbf{L^8}$ (Scheme 2).

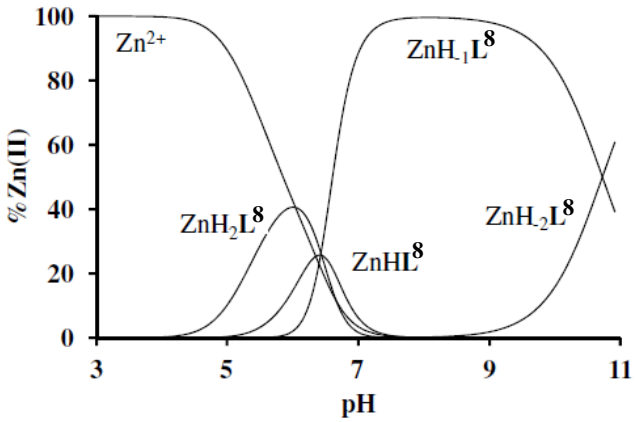

Figure 5. Speciation diagrams in Zn(II)-$\mathbf{L^8}$ 1:1 system ($c_{\mathbf{L1}} = c_{Zn(II)}$ = 0.001 M, I = 0.1 M NaCl, T = 298 K).

The formation of $ZnH_{-1}\mathbf{L}^{8}$, a dominant complex between pH 7-10, occurs through two strongly cooperative deprotonation steps ($ZnH\mathbf{L}^{8} = ZnH_{-1}\mathbf{L}^{8} + 2H^{+}$). Parallel with this process remarkable changes can be observed in the NMR spectra, which results in a very complex spectrum in the aliphatic range (Figure 6.A). This is due to the slow ligand exchange rate of $ZnH_{-1}\mathbf{L}^{8}$, and the inequivalence of all CH_2 groups related to the metal-bound ligand. The COSY spectrum (Figure 6.C) supports the strong inequivalence of CH_2 groups related to both the tren and His subunits.

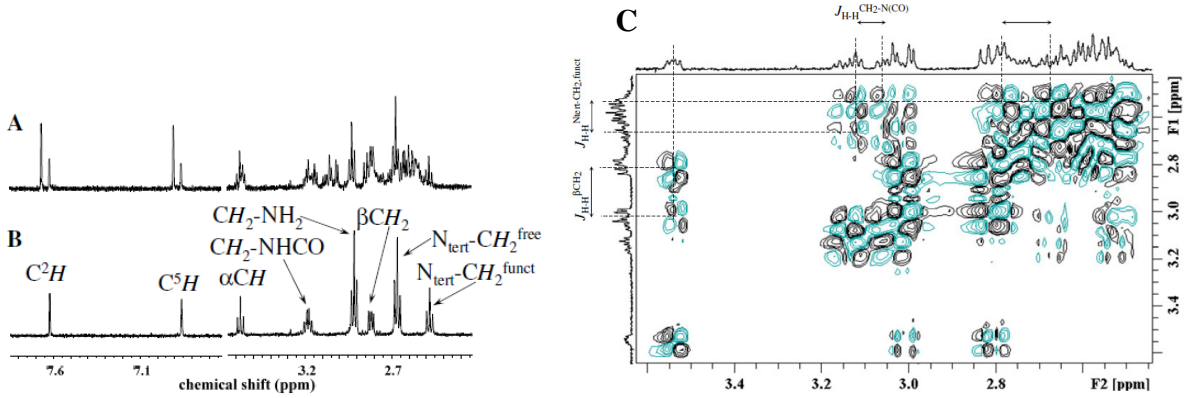

Figure 6. ^{1}H NMR spectrum of Zn(II)-$\mathbf{L}^{8}$ 1:1.5 (**A**) and 0:1 (**B**) systems at pH 8.9, and the COSY spectrum of Zn(II)-$\mathbf{L}^{8}$ 1:1 system at pH 8.6 (in H_2O/D_2O, $c_{\mathbf{L}8} = 0.0016$ M, $I = 0.1$ M NaCl, $T = 298$ K).

The slow ligand exchange rate indicates metal-promoted amide-deprotonation, while the inequivalence of all CH_2 protons suggests that all methylene-groups are part of chelate rings, *i.e.* in $ZnH_{-1}\mathbf{L}^{8}$ the metal ion is five-coordinated with trigonal bipyramidal or square pyramidal geometry, as depicted in Scheme 2. Figure 6.C clearly shows two sets of imidazole protons, the Zn(II)-bound signals are downfield shifted by 0.05 ppm as compared to the free ligand, suggesting lower electron density of the bound ring. Since the αCH signal does not show similar chemical shift difference, the coordination of the N3 imidazole nitrogen can be assumed in the fifth coordination site of the Zn(II) ion.

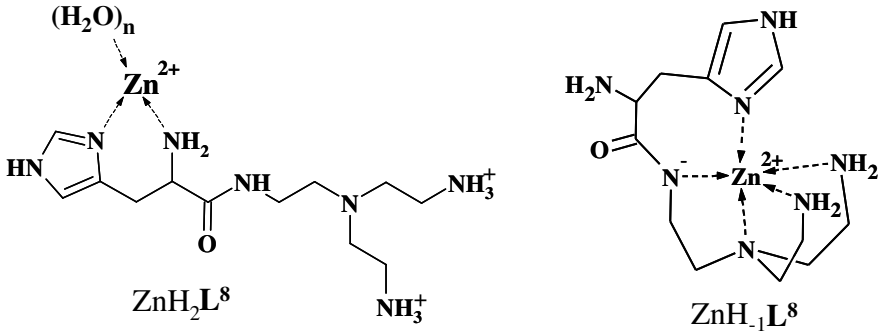

Scheme 2. Proposed structure of main Zn(II)-$\mathbf{L}^{8}$ complexes.

In presence of ligand $\mathbf{L}^{7}$ water soluble mono- and dinuclear complexes are formed (Figure 7). In the equimolar solution the formation of $ZnH_2\mathbf{L}^{7}$ and $ZnH\mathbf{L}^{7}$ results in notable broadening of the imidazole and His-βCH_2 signals (Figure 8) indicating histamine-type $\{2N_{im},NH_2\}$ and $\{2N_{im},2NH_2\}$ coordination, respectively. In $ZnH\mathbf{L}^{7}$ the *bis*-histamine-type coordination of the two histidyl-substituted leg of $\mathbf{L}^{7}$ results in inequivalency of tren N_{tert}-CH_2 groups of the substituted legs (Figure 8), caused by the formation of fused chelate rings.

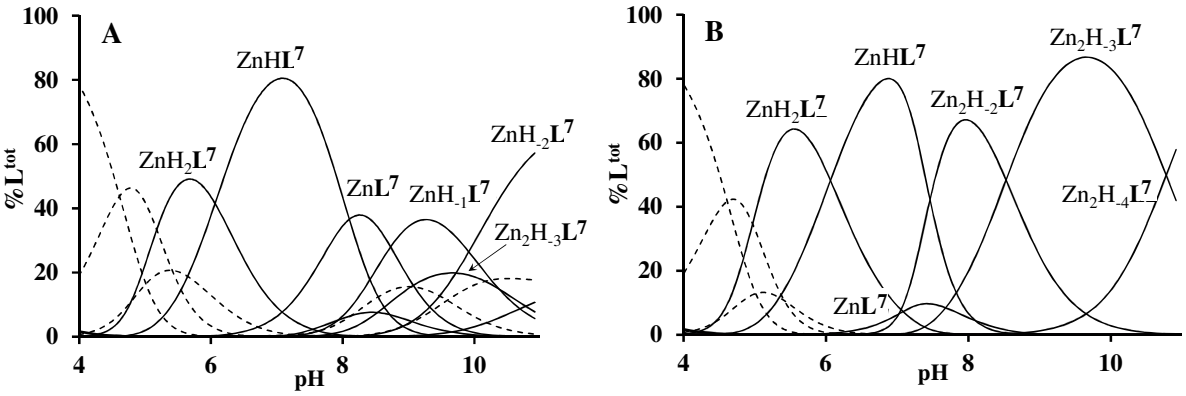

Figure 7. Speciation diagrams in Zn(II)-$\mathbf{L}^7$ 1:1 (**A**) and 2:1 (**B**) systems ($c_{\mathbf{L}^7}$ = 0.001 M, $c_{Zn(II)}$ = 0.001 and 0.002 M, I = 0.1 M NaCl, T = 298 K), dashed lines represent unbound ligand ($H_x\mathbf{L}^7$) species.

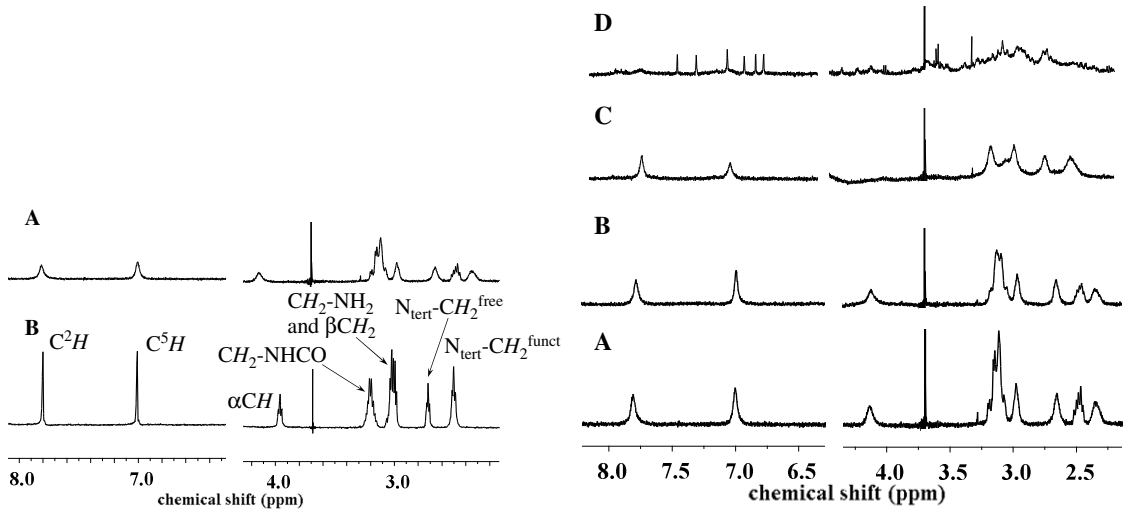

Figure 8. ^{1}H NMR spectra of the Zn(II)-$\mathbf{L}^7$ systems. Left: Zn(II)/$\mathbf{L}^7$ = 1:1 (**A**) and 0:1 (**B**) at pH 6.6 and 6.8 respectively. Right: Zn(II)-$\mathbf{L}^7$ 1:1 pH = 6.8 (**A**), Zn(II)-$\mathbf{L}^7$ 2:1 pH = 6.9 (**B**), Zn(II)-$\mathbf{L}^7$ 1:1 pH = 8.7 (**C**) and Zn(II)-$\mathbf{L}^7$ 2:1 pH = 8.6 (**D**) (in H_2O/D_2O, $c_{\mathbf{L}^7}$ = 0.0018 M, I = 0.1 M NaCl, T = 298 K).

Above neutral pH, overlapping deprotonation steps take place to result Zn$\mathbf{L}^7$, ZnH$_{-1}\mathbf{L}^7$, ZnH$_{-2}\mathbf{L}^7$ and a small amount of dinuclear species. The broadening of the NMR signals escalates in the basic pH-range, allowing to draw only limited conclusions. Indirect information, however, can be extracted: since the coordination of the amide nitrogen(s) would result in slow ligand exchange processes (see Zn(II)-$\mathbf{L}^8$), the 'extra' deprotonations must be related to the formation of mixed hydroxo-species (Zn$\mathbf{L}^7(OH)_x$).

At metal excess, three dinuclear complexes could be determined by potentiometry, with Zn$_2$H$_{-2}\mathbf{L}^7$, Zn$_2$H$_{-3}\mathbf{L}^7$ and Zn$_2$H$_{-4}\mathbf{L}^7$ compositions. Beside the monozinc(II) complexes, the presence of dinuclear species has also been confirmed by MALDI-TOF-MS measurements. The dinuclear complexes start to appear above pH 7 (Figure 7). This is in agreement with the ^{1}H NMR spectra recorded at twofold metal excess, the spectral features up to pH 7 are identical to that observed at 1/1 Zn(II)-$\mathbf{L}^7$ ratio (Figure 8). The slow ligand exchange observed

above pH 7 results the appearance of several small sharp signals in the aromatic region of the spectra (Figures 8 and 9). TOCSY and ^{1}H NMR spectra of the complexes deuterated at the imidazole C2 carbon allowed the identification of the C^2H-C^5H pairs (Figure 9) within the peak set (Figure S6.2.). The appearance of this set of signals indicates chemically different environments for the imidazole groups in the slow exchanging dinuclear complexes. Since **L**^{7} possesses only two imidazole moieties, the observed spectra imply the presence of constitutional isomers and/or oligomerization of the dinuclear complexes. Since three different environment can be identified for the imidazole rings with nearly equal populations, both above mentioned possibilities should take place. Indeed, ^{1}H DOSY (Diffusion-Ordered NMR Spectroscopy) measurements revealed that one of the three imidazole peak pairs corresponds to a slightly slower diffusion as compared to the other two, supporting the the formation of an isomer containing two ligand molecules.

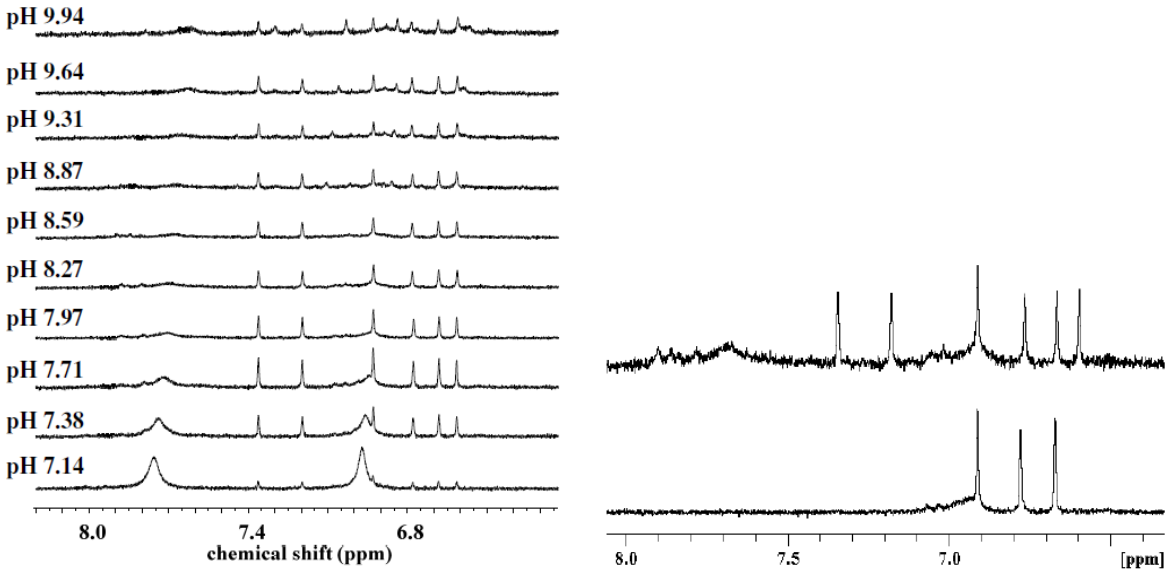

Figure 9. ^{1}H NMR spectra of Zn(II)-**L**^{7} 2:1 system. Left: pH dependence of the aromatic proton signals. Right: Aromatic region of the ^{1}H NMR spectra recorded in 100% D_2O before (up) and after (down) exchanging the labile C2H protons (pH ~ pD = 8.2).

In the Zn(II)-**L**^{6} system clear solution was obtained in the whole studied pH range at 1:1 and 1.5:1 metal-to-ligand ratio, but precipitation was observed at twofold metal ion excess. The evaluation of potentiometric data indicated the formation of complexes with ZnH_x**L**^{6} and Zn_3H_x**L**$^6_2$ stoichiometries (Figure 10), similarly to the previously reported Cu(II)-tren3his system [3]. The presence of mono- and trinuclear species was also confirmed by Maldi-TOF MS.

Above pH 5, the selective broadening of ^{1}H NMR signals of both imidazole and αCH protons indicates histamine-like coordination in ZnH**L**^{6} and Zn**L**^{6}. The participation of the third arm of **L**^{6} can also be presumed based on the pK values of the protonated complexes (pK_{ZnH_2L} = 5.42, pK_{ZnHL} = 6.49), which are lower compared to the analogous copper(II) containing complexes (pK_{CuH_2L} = 5.55, pK_{CuHL} = 6.92 [3]), according to the higher preference of zinc(II) toward regular octahedral geometry. Beside the selective broadening, the duplication of N_{tert}-CH_2 signals of the tren moiety can be also observed on the NMR spectra between pH 5 and 9, similarly to the Zn(II)-**L**^{7} 1:1 system (see Figure 8). Such duplication does not occur for the other signals, and there is no slow ligand exchange yet, therefore this is due to the magnetic inequivalence of the geminal hydrogens, caused by the formation of fused chelate rings.

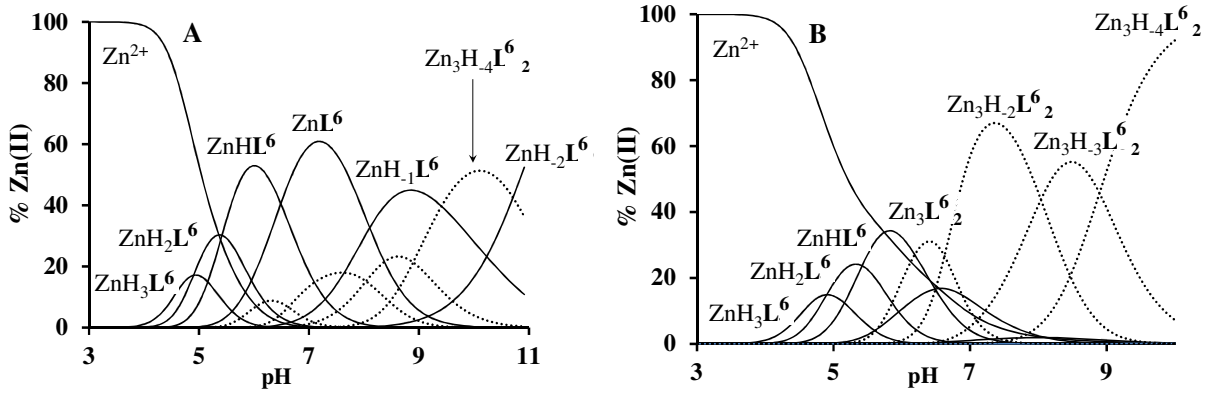

Figure 10. Speciation diagrams in Zn(II)-$\mathbf{L^6}$ 1:1 (**A**) and 1.5:1 (**B**) systems ($c_{\mathbf{L6}}$ = 0.001 M, $c_{Zn(II)}$ = 0.001 and 0.0015 M, I = 0.1 M NaCl, T = 298 K), dotted lines represent trinuclear ($Zn_3H_{-x}\mathbf{L^6_2}$) species.

Under basic conditions $Zn\mathbf{L^6}$ releases two additional protons (pK = 8.10 and 10.24). Since the formation of $ZnH_{-1}\mathbf{L3}$ and $ZnH_{-2}\mathbf{L3}$ is overlapped with those of the oligonuclear complexes, no clear structural assignment can be made for these complexes. However, deceleration of the ligand exchange does not occur at this metal-to-ligand ratio, which was observed for the tren-like coordination of zinc(II) with the participation of amide nitrogens (see $ZnH_{-1}\mathbf{L^8}$), therefore these deprotonations are more likely related to the formation of mixed hydroxo complexes ($ZnH_{-1}\mathbf{L}$=Zn**L**(OH) and $ZnH_{-2}\mathbf{L}$=Zn**L**$(OH)_2$), similarly to many other zinc(II)-peptide systems.

Interestingly, considerable amount of trinuclear complexes are formed even in equimolar solution, according to potentiometric and NMR data (Figure 10). This indicates that $\mathbf{L^6}$ is able to bind more than one zinc(II) with nearly equivalent binding affinities. The very existence of $Zn_3H_{-x}\mathbf{L^6_2}$ type complexes implies that in these species two Zn(II) ions are coordinated by two arms of the tripod, originated from the same ligand, while the third zinc(II) is coordinated by the third legs of the two ligand molecules. Such M_3L_2 type cluster formation is well known in the literature regarding tripodal ligand complexes. This process also results a significant amount of unbound $\mathbf{L^6}$ in basic solution at 1:1 metal-to-ligand ratio.

At 3:2 metal-to-ligand ratio, trinuclear complexes become dominant above pH 6 (Figure 10). Extra deprotonations begin at lower pH values compared to the mononuclear system, since in $Zn_3\mathbf{L^6_2}$ the metal ions are surrounded by less nitrogen than in $Zn\mathbf{L^6}$, therefore they are more prone to induce 'extra' deprotonations. The successive deprotonations of $Zn_3\mathbf{L^6_2}$ result in considerable deceleration of ligand exchange. Accordingly, around pH 10 (parallel with the formation of $Zn_3H_{-4}\mathbf{L^6_2}$), a number of sharp signals appear on the ^{1}H NMR spectra (Figure 11). The high number of peaks cannot be explained by the presence of differently protonated, *i.e.* the observed set of signals correspond to several different chemical environment of a single deprotonation state. The TOCSY spectrum indicates the presence of at least 7 different C^2-H/C^5-H imidazole proton pairs at pH 9.8, where ~95% of zinc(II) is bound in $Zn_3H_{-4}\mathbf{L^6_2}$.

The observed multiplication of the signals can imply either the inequivalence of imidazole protons in the trinuclear species due to the conformational differences, or the formation of oligomer complexes with different compositions ($Zn_{3n}H_{-xn}\mathbf{L^6_{2n}}$, n ≥ 1), which would result in at least minor variance in the hydrodynamic radii of these species. Pursuing this, ^{1}H DOSY measurements were performed. The results indicate the presence of several complexes with moderately different diffusion parameters, which are, however, clearly distinct from that of the free ligand (see the signals at 7.61 ppm and 6.85 ppm in Figure 12),

supporting the association of trinuclear zinc(II) complexes. Applying the approximate rule $(D_{ref}/D_x)^3 = M_x/M_{ref}$ (where D and M stands for diffusion coefficient and molar mass, ref. values: dioxane and acetonitrile), one can estimate the presence of oligomers formed by the association of 2-8 trinuclear complexes (although uncertainties must be taken into account due to the non-spherical geometry and different hydratation of the ligand and its zinc(II) complexes).

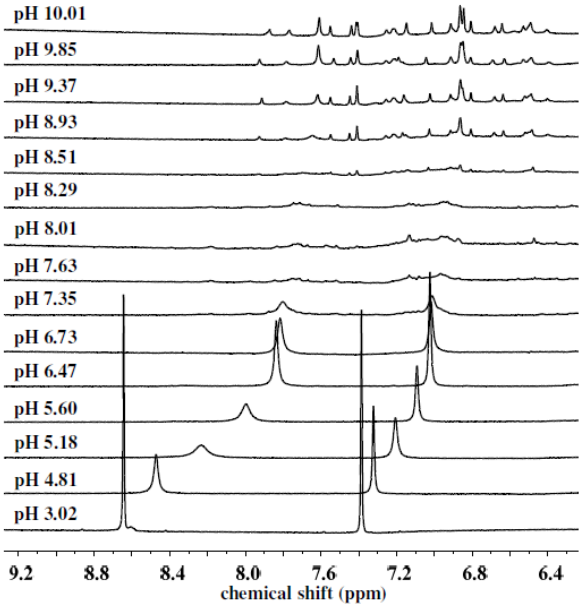

Figure 11. Aromatic region of the pH dependent ^{1}H NMR spectra of Zn(II)-$\mathbf{L^6}$ 3:2 system (in H_2O/D_2O, $c_{\mathbf{L}^6}$ = 0.0023 M, I = 0.1 M NaCl, T = 298 K).

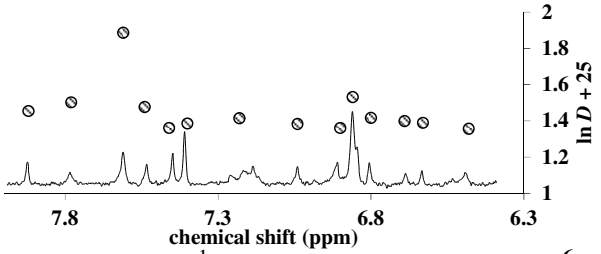

Figure 12. Aromatic region of ^{1}H NMR spectra in Zn(II)-$\mathbf{L^6}$ 3:2 system at pH 10. Secondary axis: measured diffusion coefficients by ^{1}H 2D DOSY NMR (c_L = 0.0019 M, $c_{Zn(II)}$ = 0.0027 M, I = 0.1 M NaCl, T = 298 K).

The complexity of the NMR spectra, especially in the aliphatic region, does not allow doubtless identification of the zinc(II) promoted deprotonations (which can result in the coordination of either OH^-, amide nitrogens or even imidazolato bridge) in these assembled species. However, it seems clear that the formation $Zn_3H_{-4}\mathbf{L^6_2}$ triggers the above described oligomerization, involving a major transformation in the structure of the complex. This, and the striking resemblance to the Zn(II)-$\mathbf{L^7}$ 2:1 system at basic pH (see Figures 8 and 9). One should also consider, that the formation of mixed hydroxo or amide-coordinated complexes cannot explain the some cases more than 1 ppm shift of imidazole protons. All these facts might support the formation of μ-imidazolato-bridges between the zinc(II) cores.

2.5 Mimics of small ribozymes utilizing a supramolecular scaffold (zinc(II) complexes of $\mathbf{L}^{9a\text{-}d}$ [5])

An increasing number of cases are reported, where nucleobases of a ribozyme function as general acid/base catalysts for the cleavage of phosphodiester bonds. Either, the nucleophilicity of the attacking 2′-hydroxy group is enhanced by concomitant proton transfer to a nucleobase, and/or the departure of the 5′-oxygen is facilitated by proton donation from a nucleobase. To learn more about the mechanistic details of these processes, general acid/base catalysis of RNA cleavage has been extensively studied. A possible way to learn more about the role of general acid/base catalysis in the RNA cleavage is to bring the local concentration of the general acid/base catalyst to a sufficiently high level. This can be achieved by anchoring the catalyst close to the scissile phosphodiester linkage. In our work we applied Zn(II) chelates of small azacrowns as sequence selective anchoring system, which binds strongly to the deprotonated N3 atom of a uracil base.

In the ligands $\mathbf{L}^{9a\text{-}d}$ employed, differing only in the substituent at position 6 of the triazine ring, the two UpU anchoring Zn(II)-cyclen chelates are linked to a common 1,3,5-triazine core (Figure 2). In $\mathbf{L}^{9a}$ the histamine sidearm (the third leg) has the potential to function as metal binding site, or as an additional general acid/base catalyst.

First we studied the interaction of $\mathbf{L}^{9b}$ with zinc(II). The presence of two azacrowns allow the formation of mono- and dinuclear complexes, and due the acid–base properties of the non-bonded nitrogens and coordinated water molecules, both may have several different protonation states. Interestingly, the relatively large difference between the binding constants of the first and second metal ion to $\mathbf{L}^{9b}$ (ΔlogK = 5.4) has been observed, in spite of the two identical cyclene subunits. This may indicate the binding of both cyclen rings to the first metal ion, i.e. an ‘earmuff’-like coordination in Zn$\mathbf{L}^{9b}$.

In the subsequent step the ternary complex formation with UpU has been studied. In the Zn(II): $\mathbf{L}^{9b}$:UpU 2:1:1 system our potentiometric study indicated the formation of a single very stable ternary complex ($Zn_2\mathbf{L}^{9b}$(UpU)), which is the sole species between pH 7-10. UpU fits into the scaffold created by the Zn_2L complex almost ideally, since the logK (= 9.54) for the reaction $Zn_2\mathbf{L}^{9b}$ + UpU = $Zn_2\mathbf{L}^{9b}$(UpU) is nearly twice as high as the respective constant for the process Zn(cyclen) + uridine = Zn(cyclen)(uridine), logK = 5.2.

Finally, the detailed kinetic investigation of the $Zn_2\mathbf{L}^{9}$ promoted hydrolysis of UpU resulted the following conclusions (Figure 13): the catalyzed hydrolysis of UpU is attributable to sequential specific base and general acid catalysis, with the attacking 2′-OH being deprotonated and a monoanionic phosphorane intermediate formed in a rapid preequilibrium step and proton transfer from this intermediate to the departing oxygen taking place concerted with rate-limiting P–O bond fission.

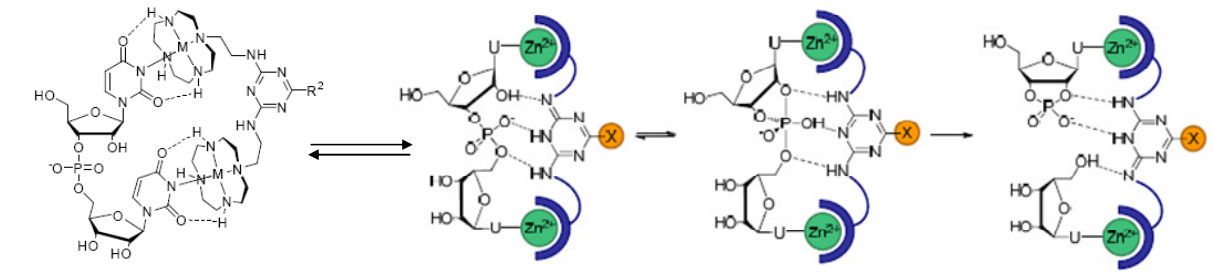

UpU : 2h (R^2 = H, M = Zn^{2+})
UpU : 2i (R^2 = 2-(1*H*-imidazol-4-yl)ethylamino, M = Zn^{2+})
UpU : 2n (R^2 = NHMe, M = Zn^{2+})
UpU : 2o (R^2 = OMe, M = Zn^{2+})

Figure 13. Proposed mechanisms for the cleavage of UpU by $Zn_2\mathbf{L}^{9a\text{-}d}$

In this kind of mechanism, the effects of the basicity of the general acid/base catalyst are opposite in the two steps: higher basicity shifts the pre-equilibrium to favor the reactive deprotonated species but at the same time retards proton transfer at the rate-limiting step. Apparently, in the present case these two effects entirely cancel each other out, indicating that the catalyst-mediated proton transfer to the leaving group must be nearly complete at the rate-limiting step. Together with the exocyclic amino functions at C2 and C4, N3 of the triazine ring forms a conjugated network of hydrogen bond donors and acceptors that, upon tautomerization, may abstract and release a proton at any of the three nitrogen atoms. More specifically, this network could mediate proton transfer from the attacking 2′-OH to the phosphorane intermediate and, ultimately, to the departing 5′-oxygen, closely mimicking the proposed action of the catalytic guanine moiety in hammerhead and hairpin ribozymes.

2.6 A novel 1,3,5-triaminocyclohexane-based tripodal ligand forms a unique tetra(pyrazolate)-bridged tricopper(II) core: solution equilibrium, structure and catecholase activity (copper(II) complexes of $\mathbf{L^{10}}$ [6]).

Derivatization of the legs of tripodal platforms provides additional donor site(s), may influence the steric environment around the metal centre, as well as may help to introduce additional functions, such as substrate binding or activation. The preorganization of the tripodal scaffold can be substantially increased by allosteric metal ion(s), which may create high affinity binding site(s) for the catalytic metal ion(s). In order to develop such an oligonuclear core by allosteric interaction, the N-substituted tach ligand needs to accommodate additional metal binding site(s), for which purpose pyrazole-substituted tach derivarives are appropriate candidates. Pyrazolate-bridged metal complexes have received significant attention over recent decades, among others, due to their unique ability to self-assemble into supramolecular architectures.

Our aim was to explore the combined advantages of the preorganized structure of tripodal scaffolds and the metal bridging ability of pyrazole rings in order to develop a new oligometallic core under allosteric control, which may potentially mimic the function of oxidase enzymes. Accordingly, we synthesized the ligand $\mathbf{L^{10}}$ and studied its complexes formed with copper(II) both in solution and in solid state. Spectroscopically calibrated, hybrid DFT calculations were also used to gain deeper insights into the electronic structure and spin-coupling scheme by considering both ferro- and antiferromagnetic ground states. To screen the enzyme mimetic properties of the copper(II) complexes their catecholase activity was studied by using 3,5-di-tert-butylcatechol (H_2dtbc) as model substrate.

In the copper(II)-$\mathbf{L^{10}}$ system two mononuclear (Cu$\mathbf{H_{}L^{10}}$, Cu$\mathbf{L^{10}}$) and three trinuclear ($Cu_3H_{-x}\mathbf{L^{10}}_2$, x = 2, 3, 4) complexes were identified in solution by combined evaluation of potentiometric, UV-VIS, and EPR data. The mononuclear Cu$\mathbf{L^{10}}$ complex is highly stable, nevertheless it transforms into trinuclear complexes even in equimolar Cu(II):$\mathbf{L^{10}}$ solution. Parallel with the development of trinuclear complexes, intense charge transfer bands appear around 400–500 nm, indicating the formation of pyrazolate-bridged complexes. The crystal structure of $[Cu_3H_{-4}\mathbf{L^{10}}_2](ClO_4)_2\times5H_2O$ reveals the formation of a unique trinuclear complex that features a tetra(pyrazolate)-bridged linear tricopper(II) core (Figure 14). The two peripheral copper(II) ions have slightly distorted square pyramidal geometry. The four pyrazole rings bound to the two peripheral copper(II) ions are deprotonated and create a Jahn-Teller distorted flattened tetrahedral environment for the central copper(II).

The complete transformation of Cu$\mathbf{L^{10}}$ into $Cu_3H_{-4}\mathbf{L^{10}}_2$ in equimolar Cu(II):$\mathbf{L^{10}}$ solution is noteworthy, especially considering that its formation results in the liberation of a bound ligand $3Cu\mathbf{L} = Cu_3H_{-4}\mathbf{L}_2 + \mathbf{L} + 4H^+$, despite the high stability of Cu$\mathbf{L^{10}}$. Therefore, the

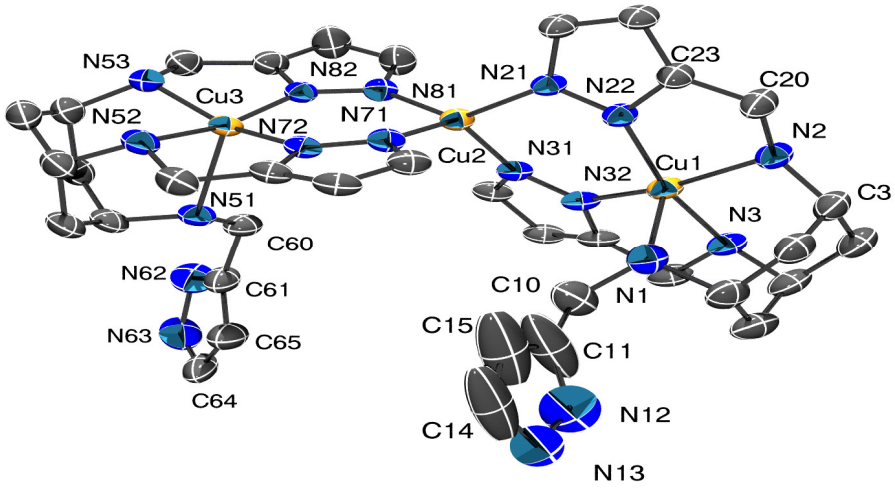

Figure 14. ORTEP view (40%) of the trinuclear complex $[Cu_3H_{-4}\mathbf{L}^{10}_2](ClO_4)_2\times 5H_2O$ with partial numbering scheme. Perchlorate counter ions, water molecules as well as hydrogen atoms were omitted for clarity

formation of the trinuclear complex is thermodynamically highly favoured above pH 7, and can be regarded as a pH-driven self-assembly. Since the coordination of copper(II) ion to pyrazole N(1) nitrogens is a pre-requisite for the deprotonation of N(2)H protons at around the neutral pH range, the formation of the trinuclear complex is under the allosteric control of the two terminal copper(II) ions.

Hybrid DFT calculations provided additional details about the geometric and electronic structures of the trinuclear complex showing the preference of the antiferromagnetically coupled ground state with $S_t = 1/2$ ground state.

The triply deprotonated trinuclear complex is a highly efficient catechol oxidase mimic, which shows a surprisingly low pH optimum around pH = 5.6. Since the mononuclear Cu**L** species is not able to promote the oxidation of 3,5-di-tert-butylcatechol, we assume that the central copper(II) ion with unsaturated coordination sphere has a fundamental role in binding and oxidation of the substrate.

2.7 Tailoring the local environment around metal ions: solution chemical and structural study of some multidentate tripodal ligands (Mn(II), Cu(II) and Zn(II) complexes of $\mathbf{L}^{11}$, $\mathbf{L}^{12}$, $\mathbf{L}^{16}$ and $\mathbf{L}^{17}$ [7])

The favourable and preorganized spatial distribution of donor atoms in tripodal ligands has been long time recognised and applied to develop metal ion chelators for a variety of purposes. In this work we studied the metal complexes of some tach and tren derivatives. The substitution of these well-known tripodal platforms may provide additional donor site(s), may influence the steric environment around the metal centre or may help to introduce further metal binding site(s) in order to create polynuclear complexes. Accordingly, these polydentate tripodal ligands are proved to be versatile building blocks for metal-organic-frameworks, efficient metal sequestering agents and artificial enzymes.

$\mathbf{L}^{11}$ and some of its derivatives are promising chelators of $^{64/67}$Cu for radiotherapeutic uses, moreover $\mathbf{L}^{11}$ and $\mathbf{L}^{16}$ are cytotoxic metal chelators with potential anti-tumor activity. $\mathbf{L}^{11}$ induces inhibition of ferritin synthesis, and triggers activation of the CHK kinases, leading to cell-cycle arrest in G_2, a radiosensitive phase of the cell cycle. The intracellular chelation of zinc as well as iron, but not copper, may play a fundamental role in the apoptosis induced by

$\mathbf{L}^{11}$ and its derivatives. Accordingly, the apoptotic caspases 9 and 3 was blocked in cells pre-treated with either iron or zinc.

Although both $\mathbf{L}^{11}$ and $\mathbf{L}^{16}$ have been designed for efficient metal ion binding, and a number of crystal structures are available for their metal complexes, thermodynamic data on the stability of these complexes are very scarce. To our knowledge, no solution equilibrium or detailed solution structural study is reported for $\mathbf{L}^{11}$, and in the case of $\mathbf{L}^{16}$ stability constants are available only for the Cu(II) and Zn(II) complexes at I = 1M.

Due to the favourable position of pyridine nitrogens of $\mathbf{L}^{11}$ and $\mathbf{L}^{16}$, these ligands encapsulate the metal ions by fused chelate rings, which is probably one of the main reasons of their efficient metal binding ability. This encapsulating effect is not present in the cases of 3-pyridylmethyl-substituted derivatives of tach and tren ($\mathbf{L}^{12}$ and $\mathbf{L}^{17}$). Although the positions of pyridine nitrogens in these ligands are not appropriate for the coordination to metal ions already bound to the tripodal platform, it may be advantageous in the construction of oligonuclear complexes. Indeed, the position of the pyridine nitrogens in $\mathbf{L}^{12}$ and $\mathbf{L}^{17}$ may allow the formation of supramolecular structures or metal-organic frameworks. In addition, the steric and aromatic properties of pyridine rings of $\mathbf{L}^{12}$ and $\mathbf{L}^{17}$ can be also advantageous to develop enzyme mimics. The Cu(tach)(OH) complex is an efficient model of hydrolytic enzymes, but it readily transforms into the inactive dihydroxo-bridged $[Cu_2(tach)_2(OH)_2]$ dimmer. N-alkylation of tach suppress the formation of the inactive dimer species, therefore these complexes efficiently promote the hydrolysis of both bis(4-nitrophenyl) phosphate (bnpp) and DNA. In the Cu(II)-$\mathbf{L}^{12}$ system the formation of the inactive dimer would be unfavourable, too, and the non-coordinating pyridine rings may enhance the substrate binding to the hydrolytically active species.

To this end, beside $\mathbf{L}^{11}$ and $\mathbf{L}^{16}$ we also synthesized two new tripodal ligands $\mathbf{L}^{12}$ and $\mathbf{L}^{17}$, and studied Mn(II), Cu(II) and Zn(II) complexes in both solution and solid state. The combined evaluation of potentiometric, UV-VIS, NMR and EPR data allowed concluding both thermodynamic and structural information on the complexes formed in solution.

During our work two new crystal forms of [Zn($\mathbf{L}^{11}$)] complex cation was crystallized and their structure determined: [Zn($\mathbf{L}^{11}$)]×$(ClO_4)_2$×O (**1**) crystallized in a monoclinic $P2_1/n$ space group and [Zn($\mathbf{L}^{11}$)]×(ClO_4)×Cl (**2**) in trigonal crystal system, R-3c space group. The copper(II) complex [Cu($\mathbf{L}^{11}$)]×$(ClO_4)_2$×H_2O (**3**) crystallized in $P2_1/n$ space group (Figure 15). In all cases, the coordination sphere of metal ions is best described as a distorted octahedron. The different counter ions affected not only the arrangement of the crystal lattice but the conformation of $\mathbf{L}^{11}$ around the metal ions, as well. In the crystals of **1, 3** the three 2-pyridylmethyl arms have different conformation. In contrary, in **2** a C_3 trigir goes through the Zn(II) ion and the asymmetric unit contains one pyridine arm of the ligand.

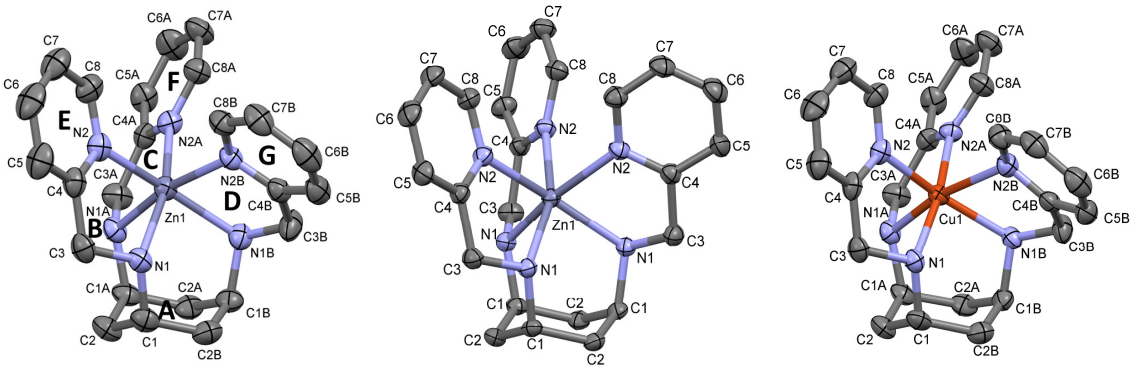

Figure 15. Molecular structures of the metal complex cations of **1**, **2** and **3** (from left to right). Hydrogens are omitted for clarity.

The comparative evaluation of our solution chemical and spectroscopic data indicated that $\mathbf{L}^{11}$ and $\mathbf{L}^{16}$ offer high thermodynamic stability, and a variety of coordination environment/geometry for manganese(II), copper(II) and zinc(II). The speciation of the Cu(H$\mathbf{L}^{11}$) complex shows a maximum around pH 1.7, while Cu($\mathbf{L}^{11}$) is the solely species in the solution above pH 4 (Figure 16). The pH-dependent Vis/NIR and EPR spectra of the copper(II)-$\mathbf{L}^{11}$ system indicated square pyramidal geometry with strong apical coordination in Cu(H$\mathbf{L}^{11}$). In solution the complex Cu($\mathbf{L}^{11}$) has distorted octahedral environment, as was observed in the crystal structure of complex **3**.

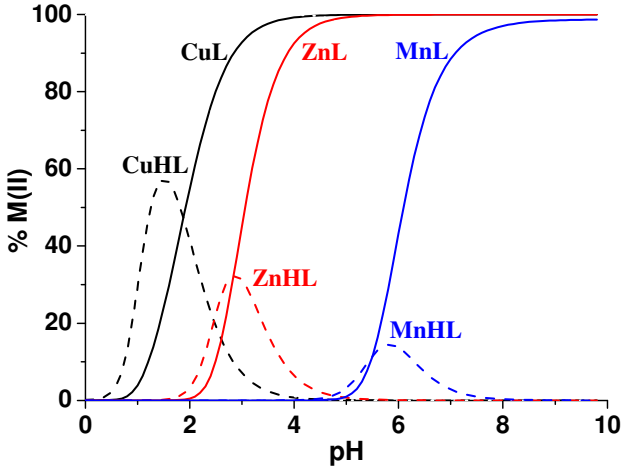

Figure 16. Speciation diagram of the M(II)-$\mathbf{L}^{11}$ complexes (T = 298 K, I = 0.1 M NaCl, [M^{2+}] = [$\mathbf{L}^{11}$] = 0.002 M, the curves of the uncomplexed metal ions have been deleted for clarity).

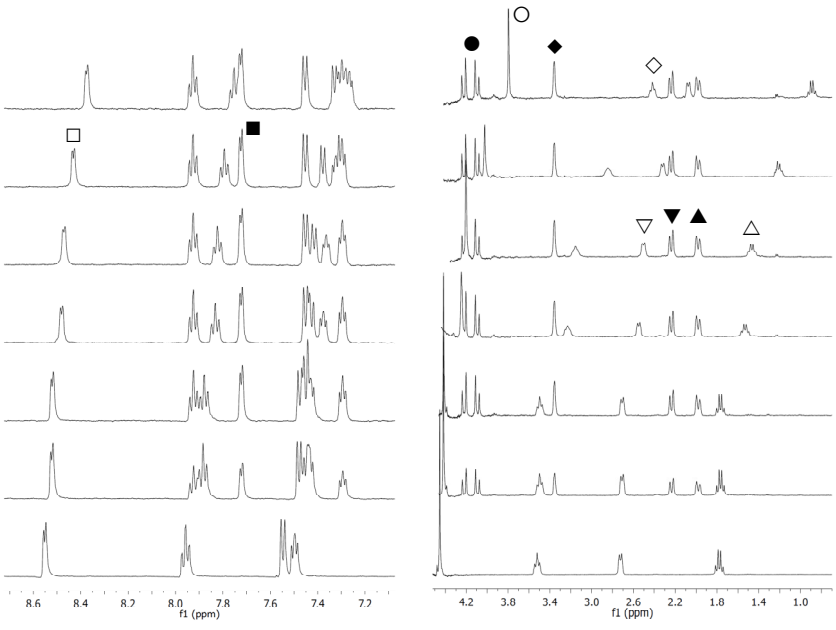

Figure 17. The pH-dependence of ^{1}H-NMR spectra of tachpyr in the presence of zinc(II) ([Zn^{2+}] = 0.002 M, [tachpyr] = 0.003 M; squares: aromatic protons next to N_{pyr}, circles: benzylic protons, rhombus: CH of cyclohexane ring, triangles: inequivalent CH_2 of cyclohexane ring of the free (open) and bound (filled) ligand).

In the zinc(II)-tachpyr system two complexes can be identified, too. The species Zn(H$\mathbf{L}^{11}$) is only a minor complex around pH 3, and Zn($\mathbf{L}^{11}$) is a dominant one above pH 5, which indicates high thermodynamic stability. The ligand exchange process of Zn($\mathbf{L}^{11}$) is slow on the NMR time-scale (Figure 17). The important differences in the spin coupling pattern between the free and bound ligand clearly show the switch between the two chair conformations (triequatorial NH → triaxial NH). Although the triaxial conformer is energetically unfavoured in the free ligand, it is the preferred one in metal complexes of all tach derivatives. In accordance with earlier reports, the single set of signals observed for this slow exchanging species indicate C_3 symmetry, the chemical inequivalence of benzylic protons (~ 4.16 ppm) shows conformational rigidity even within the 2-pyridylmethyl arms. All these facts, together with the significant chemical shift difference of protons close to the nitrogen atoms in the bound and unbound ligand suggest tight 6N-coordination around zinc(II), as seen in the crystal structures of **1** and **2**.

Earlier RP-HPLC study on the aqueous Mn(II)-$\mathbf{L}^{11}$ system indicated nearly complete dissociation at pH 5.5. In agreement with this finding, our potentiometric data indicated the formation of Mn(H$\mathbf{L}^{11}$) and Mn($\mathbf{L}^{11}$) started at pH 4.6, and the latter species are the solely complex only above pH 8 (Figure 16). Consequently, the Mn(tachpyr) complex is considerably less stable than the corresponding copper(II) or zinc(II) species, according to the Irwing-Williams series.

The formation constants of copper(II)- and zinc(II)-$\mathbf{L}^{16}$ complexes have been already published for 1 M KNO_3 background electrolyte. In order the have comparable data with other formation constants reported in this work, we repeated the solution equilibrium study of these systems in 0.1 M NaCl solutions (Figure 18), and complemented by pH-dependent Vis/NIR and ^{1}H NMR studies. The Vis/NIR spectrum of Cu(H$\mathbf{L}^{16}$) is close to that of Cu(H$\mathbf{L}^{11}$), including the low energy transitions around 850 nm, indicating square pyramidal geometry in both species. On the other hand, the spectrum of Cu($\mathbf{L}^{16}$) is completely different from that of the 6N coordinated Cu($\mathbf{L}^{11}$), and indicates an intermediate geometry between square pyramidal and trigonal bipyramidal.

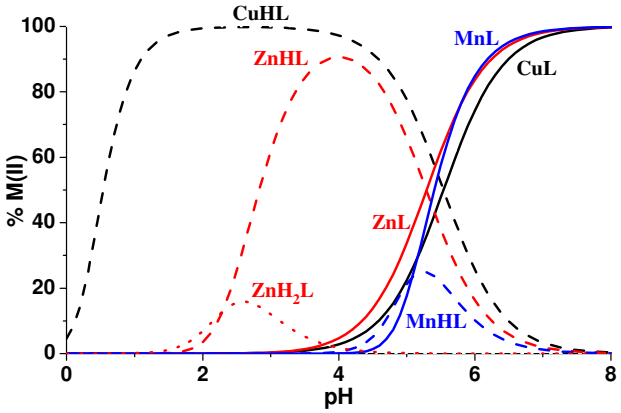

Figure 18. Speciation diagram of the M(II)-$\mathbf{L}^{16}$ complexes (T = 298 K, I = 0.1 M NaCl, [M^{2+}] = [$\mathbf{L}^{16}$] = 0.002 M, the curves of the uncomplexed metal ions have been deleted for clarity).

In the presence of zinc(II), the formation of Zn($H_2\mathbf{L}^{16}$), Zn(H$\mathbf{L}^{16}$) and Zn($\mathbf{L}^{16}$) was detected, similarly to the earlier report. Zn(H$\mathbf{L}^{16}$) is a dominant species at pH 4, its deprotonation is complete at pH 7. The ^{1}H NMR data revealed slow ligand exchange on the NMR time-scale for both Zn(H$\mathbf{L}^{16}$) and Zn($\mathbf{L}^{16}$) complexes (Figure 19). The proton signals, especially the methylene protons of Zn(H$\mathbf{L}^{16}$) are considerably broadened. Since the signals

of the free ligand are sharp in the Zn(II)-$\mathbf{L}^{16}$ system at any pH, the observed broadening for Zn(H$\mathbf{L}^{16}$) is due to the conformational changes, likely induced by intramolecular proton-transfer processes, *i.e.* the proton 'hops' between the secondary nitrogens.

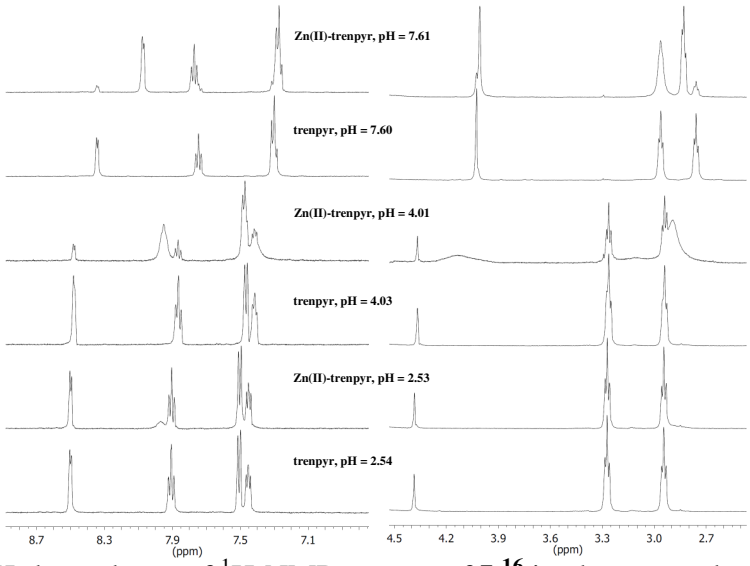

Figure 19. The pH-dependence of ^{1}H-NMR spectra of $\mathbf{L}^{16}$ in absence and presence of zinc(II) ([Zn^{2+}] = 0.002 mM, [tachpyr] = 0.0024 M, 298 K)

The signals belonging to Zn($\mathbf{L}^{16}$) complex are rather sharp (Figure 19). Since in the crystal structure of [Zn($\mathbf{L}^{16}$)]$(ClO_4)_2$ (reported in the literature) one of the pyridine rings is not coordinated, and therefore the ligand is asymmetrically bound, it is surprising that only one set of signals is present for the three 'legs' on the NMR spectrum of the slow exchanging Zn($\mathbf{L}^{16}$). This indicates C_3 symmetry of the complex, and either seven-coordinated {N_{tert},3NH,3N_{pyr}} or six-coordinated {3NH,3N_{pyr}} type binding mode of $\mathbf{L}^{16}$. In the case of zinc(II) the latter is more likely, and this binding mode is present in the Zn(II) complex of the closely related Schiff-base derivative of $\mathbf{L}^{16}$. Furthermore, the aromatic protons beside the pyridine N (C^6H), despite the expectations, are considerably more upfield shifted (7.48 ppm) in Zn(H$\mathbf{L}^{16}$) than in Zn($\mathbf{L}^{16}$) (8.07 ppm), which indicates notable changes in the coordination environment of zinc(II) during the deprotonation. All these facts may support the {3NH,3N_{pyr}} type coordination in Zn($\mathbf{L}^{16}$).

In presence of manganese(II) only two species were detected (Figure 18). The complex Mn(Htrenpyr) is a minor complex around pH 5, its deprotonation results in Mn(trenpyr), which is the solely species above pH 7.

The significant differences between the deprotonation of CuHL/ZnHL complexes of $\mathbf{L}^{11}$ and $\mathbf{L}^{16}$ are noteworthy (compare Figures 16 and 18), which is, however, does not apply for the MnHL species. This is due to the different denticity of $\mathbf{L}^{11}$ and $\mathbf{L}^{16}$, as well as the different coordination geometry of their metal complexes. In the cases of $\mathbf{L}^{11}$ complexes, the deprotonation of the 5N coordinated MHL complexes results in the increase of coordinated nitrogen donors, i.e. the metal promoted deprotonation is favoured. In contrast, in the copper(II)- and zinc(II)-$\mathbf{L}^{16}$ complexes, the coordination number is unchanged during the MHL $\rightarrow$ ML deprotonation, therefore it is less favoured since the incoming secondary NH should displace an already bound nitrogen from the coordination sphere. On the other hand, our equilibrium data indicate that the process M(Htrenpyr) = M(trenpyr) + H^+ is more favoured for Mn(II) than for Zn(II) or Cu(II) (pK = 5.08, 5.23 and 5.56, respectively), despite the striking differences in the stability of the corresponding M($\mathbf{L}^{16}$) complexes. Since manganese(II) is the weakest Lewis-acid among these metal ions, the above order of pKs is

unusual, and suggests that the coordination of secondary NH-group induces some additional stabilization in the case of Mn(II). In this respect, it is worth noting that in the crystal structure of [Mn($\mathbf{L}^{16}$)]$(PF_6)_2$ the metal ion is seven coordinated. The above mentioned additional stabilization is most likely provided by the chelate coordination of the third NH-group and pyridine nitrogen on the same 'leg', *i.e.* the complex Mn(trenpyr) is seven-coordinated ({N_{tert},3NH,3N_{pyr}}) in solution, too. Our equilibrium data indicate that $\mathbf{L}^{11}$ is more efficient zinc(II), nearly similar copper(II), and less efficient manganese(II) chelator than $\mathbf{L}^{16}$. Considering the energy demanding switch between the (triequatorial NH → triaxial NH) conformations of $\mathbf{L}^{11}$ and the conformational flexibility of $\mathbf{L}^{16}$, these data are somewhat surprising, and is very likely due to the encapsulating effect of the more rigid tachpyr skeleton. On the other hand, the observed relative binding preference of $\mathbf{L}^{11}$ for zinc(II) is probably related to the observation that zinc(II) is one of the principal metals targeted by $\mathbf{L}^{11}$ in cells.

The closely related new ligands, $\mathbf{L}^{12}$ and $\mathbf{L}^{17}$ have been designed to form oligonuclear complexes. Indeed, we obtained a three dimensional metal-organic framework (MOF) with copper(II)/$\mathbf{L}^{17}$ ratio of 11/6. The cubic structure is based on distinct copper(II) containing secondary building units (SBU) in the nodes and (3-pyridylmethyl)amino groups at the edges forming a high symmetry MOF. The formation of this MOF is explained by the strong metal binding ability of all nitrogens of $\mathbf{L}^{17}$, and by the position of pyridine nitrogens which are not able to form chelate rings with the secondary/tertiary amines. In this way, all $\mathbf{L}^{17}$ molecules are bound to four different copper(II) ions (Figure 20.a). This structural feature results in the formation of an infinite $(Cu_{11}\mathbf{L}^{17}{}_6)_n$ polymer, in which each copper(II) has a coordinated chloride, and the counter ions are also chlorides. Two of these polymers create an interpenetrated network in the crystal structure. Beside the rigid framework, more than 20% of the unit cell volume consists of separated voids. In these cavities the remaining electron density could be well modelled by chloride ions, solvent ethanol and water molecules hence the void volume of the unit cell is 1.7%, 326 $Å^3$ in the refined complete structure.

Within this metal-organic framework three distinctly different copper centres or SBUs can be identified. The first one has slightly distorted trigonal bypiramidal geometry (τ = 0.885), and this type of copper is bound to all tren-like moieties (Figure 20.a). The second has nearly perfect square pyramidal geometry (τ = 0.053) with four pyridine nitrogens in its basal plain (Figure 20.b). The distance of the metal ion from the mean plane of the four nitrogens is 0.3 Å. All pyridine rings originated from different ligand molecules, *i.e.* this copper(II) centre connects four type 1 SBUs, and is therefore responsible for the formation of the hexanuclear subunits with a large inside cavity (Figures 20.d).

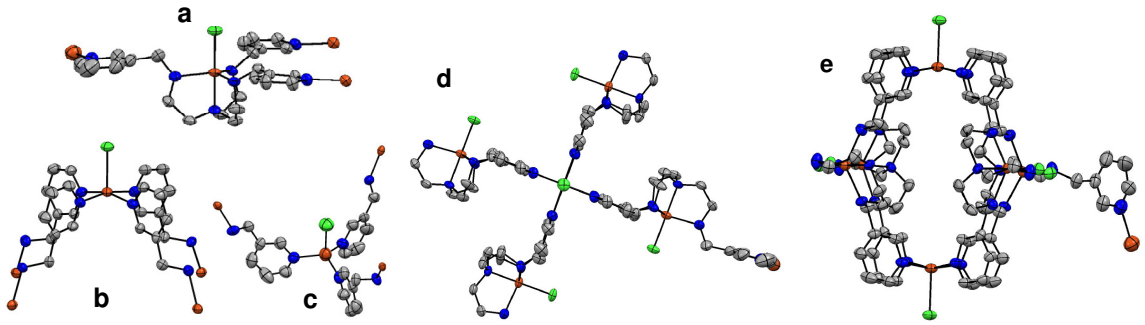

Figure 20. Structure of the three types of Cu(II) centres in the **1**MOF (a,b,c), as well as the top (d) and side view (e) of the $Cu_6(\mathbf{L}^4)_4$ subunit (for clarity, the third leg is shown only for one of the ligands, together with a tetrahedral copper which connects the hexanuclear subunits).

The third type of copper centre has distorted tetrahedral geometry (Figure 20.c) constituted by three pyridine nitrogens and a chloride ion. Distances of the metal ion and the centroid of the tetragon to the N3 plane are 0.4 and 0.7 Å, respectively. The three coordinated pyridine rings belong to three different hexanuclear subunits, consequently these copper centres create the 3D MOF. Two of these 3D polymers are interlaced and form an interpenetrated network with special topology in the crystal structure.

Altogether the unit cell contains 24 tren3pyr ligands with 168 nitrogen donors, all of them are coordinated, and 44 copper(II) ions (24, 12 and 8 of type 1, 2 and 3, respectively). The shortest Cu··Cu distances are 6.796 Å. Several mononuclear structures related to type 1 and 2 copper(II) centres can be found in the literature, but only copper(I) complexes are reported to have similar coordination sphere to type 3 SBU. The structures of individual SBUs are close to their mononuclear counterparts, *i.e.* despite the extensive coordination connectivity within this MOF the whole structure is surprisingly unstrained.

In solution only mononuclear complexes are formed with $\mathbf{L}^{12}$ and $\mathbf{L}^{17}$. The Vis/NIR (d-d transitions at 692 and ~ 1050 nm) and EPR parameters of the Cu($\mathbf{L}^{12}$) complex, are very similar to those of some N-alkylated tach derivatives, and indicate square pyramidal geometry, which is enforced by the facial coordination of the ligand. As expected, the presence of 3-pyridylmethyl legs prevent the formation of the dihydroxo-bridged dicopper complex formed with tach, and above pH 7 two mononuclear mixed hydroxo-complexes (Cu($\mathbf{L}^{12}$)(OH) and Cu($\mathbf{L}^{12}$)$(OH)_2$) are formed (Figure 21). The deprotonations of the coordinated water molecules (pK = 7.94 and 9.77) resulted in slight blue-shift of the Vis/NIR (Cu($\mathbf{L}^{12}$)(OH): 650 and ~ 900 nm; Cu($\mathbf{L}^{12}$)$(OH)_2$: 640 and ~ 900 nm) and EPR spectra, suggesting that the square pyramidal geometry is retained in these species, too. The relatively open coordination sphere of Cu($\mathbf{L}^{12}$)(OH) species is favourable from the point of view of hydrolytic catalysis. Indeed, we observed notable hydrolytic activity for the mono-hydroxo species against bis(*p*-nitrophenyl) phosphate (bnpp), an activated phosphodiester (Figure 21). The water molecule in the fifth position of copper(II) can be easily replaced by the substrate, and the copper-bound hydroxide ion may act as an intramolecular nucleophile. The initial rate of the hydrolysis as a function of bnpp concentration shows saturation kinetics. The treatment of these data, using the Michaelis-Menten model, yielded the following parameters: k_{cat} = (3.0±0.4)×10^{-5} s^{-1} and K_M = (4.2±0.8) mM.

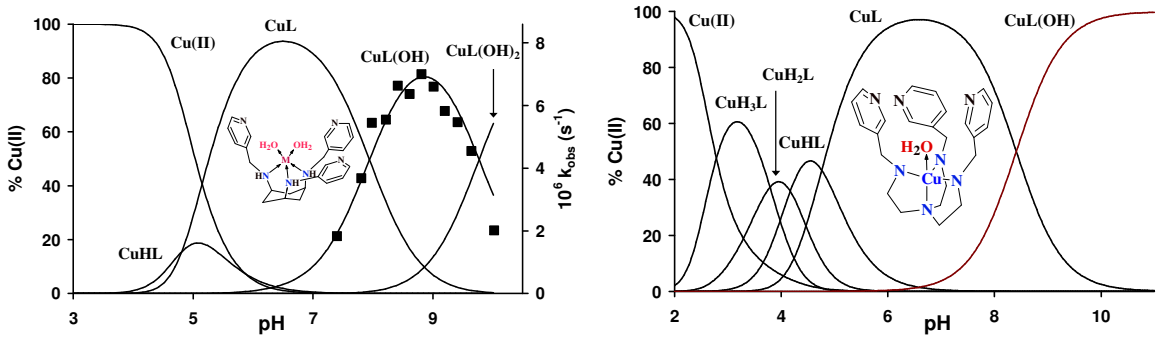

Figure 21. Left: speciation diagram of the copper(II)-$\mathbf{L}^{12}$ complexes ([Cu^{2+}] = [$\mathbf{L}^{12}$] = 0.001 M, T = 298 K, *I* = 0.1 M NaCl in 60% (w/w) dmso-water) and the pH - k_{obs} profile (■) of the bnpp hydrolysis ($[bnpp]_{ini}$ = 0.002 M); Right: Speciation diagram of the copper(II)-$\mathbf{L}^{17}$ complexes ([Cu^{2+}] = [$\mathbf{L}^{17}$] = 0.002 M, T = 298 K, *I* = 0.1 M NaCl).

L^{17} forms more stable complexes with copper(II) and zinc(II) than $\mathbf{L}^{17}$, due to the four available nitrogens for metal ion binding of the tripodal platform. In the solution of copper(II)

and $\mathbf{L}^{17}$ only mononuclear complexes ($Cu(H_x\mathbf{L}^{17})$, x = 3, 2, 1, 0, -1) have been observed (Figure 21). At two fold metal ion excess over $\mathbf{L}^{17}$ precipitate detected at pH 4-5, which prevented the equilibrium study. This precipitate was than recrystallized from ethanol to obtain complex **4**. According to the relatively high stability of $\mathbf{L}^{17}$ complexes, their formation start at pH 2 and after three overlapped deprotonations the $Cu(\mathbf{L}^{17})$ species formed, a dominant complex around pH 7 (Figure 21). During these processes the Vis/NIR and room temperature EPR spectra show identical spectral pattern. Although, the parameters of EPR spectra measured at 77 K (Figure 22) show some subtle variations with pH, they are essentially similar. Both the typical d-d bands and the 'reversed' low temperature EPR spectra ($g_z > g_x \sim g_y$, *i.e.* the complexes have a ground state with an unpaired electron in the d_{z2} orbital) indicate trigonal bipyramidal geometry in $Cu(H_x\mathbf{L}^{17})$, x = 3, 2, 1, 0. It means that the metal ion is bound to the four nitrogens of the tren-like subunit already in $Cu(H_3\mathbf{L}^{17})$, and the successive deprotonations are related to non-coordinating pyridine rings. Although, the p*K* values of these deprotonations (p*K* = 3.79, 4.17 and 4.76) are somewhat higher than those of the free ligand, this is due to the higher electron withdrawing effect of the protonated secondary amino nitrogens as compared to the neutral (and metal ion coordinated) ones.

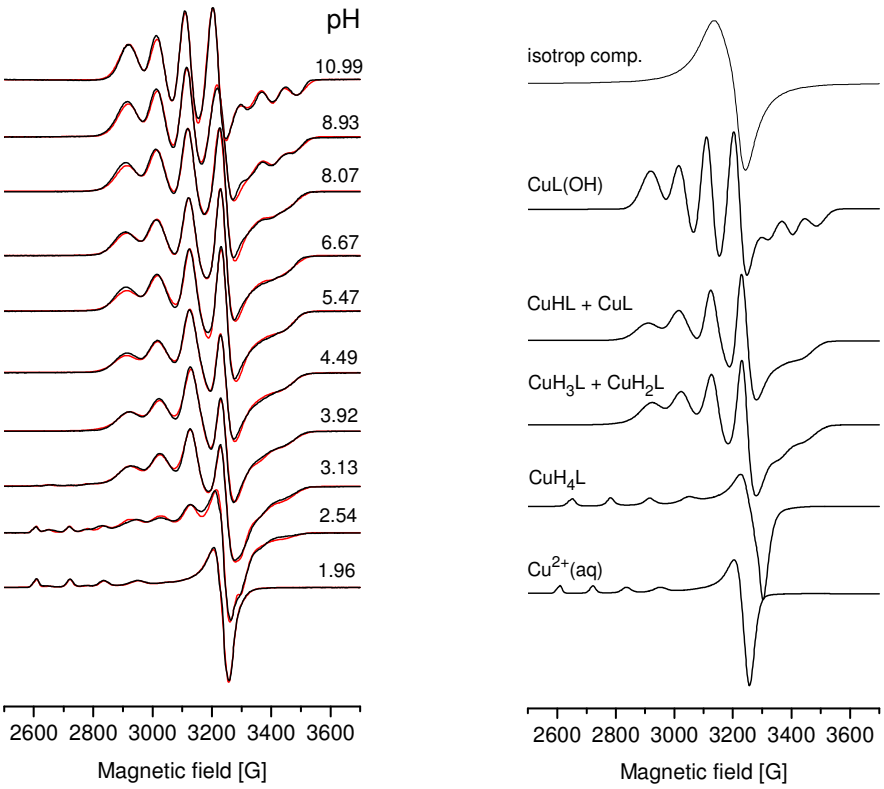

Figure 22. Experimental (black) and simulated (red) EPR spectra of the copper(II)-$\mathbf{L}^{17}$ systems at 77 K ($[Cu^{2+}] = [\mathbf{L}^{17}] = 0.003$ M). The calculated component spectra of the main species are also shown on the right.

Above pH 7 a single deprotonation was observed which resulted in the formation of $Cu(\mathbf{L}^{17})(OH)$. Both Vis/NIR and EPR spectra show considerable differences between $Cu(\mathbf{L}^{17})$ and $Cu(\mathbf{L}^{17})(OH)$, although the typical features of trigonal bipyramidal geometry are retained.

In presence of zinc(II) two major species forms, Zn($\mathbf{L}^{17}$) between pH 6-8, and Zn($\mathbf{L}^{17}$)(OH) above pH 8. Both complexes have slow ligand exchange processes on the NMR-timescale (Figure 23). In Zn($\mathbf{L}^{17}$) the signals of ethylene protons are considerably broadened, those of the benzylic protons are completely disappeared from the spectra. On the other hand, at higher pH the signals are narrowed, and the benzylic protons (~ 4.1 ppm) are clearly visible on the spectrum of Zn($\mathbf{L}^{17}$)(OH), indicating conformationally less labile pyridine rings in this species (see later). The signals of aromatic protons are less affected by such dynamic processes, implying that zinc(II) is coordinated only by the four nitrogens of the tren-like subunit, similarly to the corresponding copper(II) complexes.

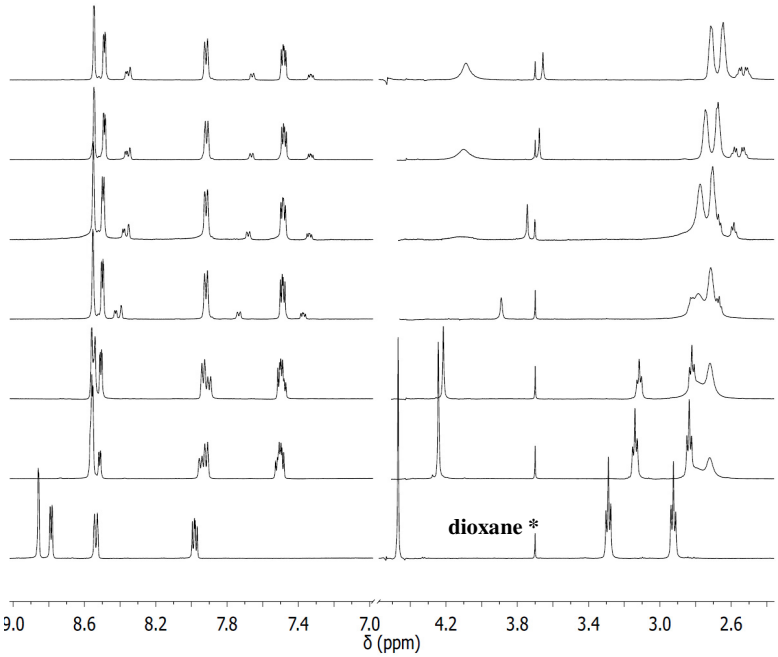

Figure 23. The pH-dependence of ^{1}H-NMR spectra of $\mathbf{L}^{17}$ in the presence of zinc(II) ([Zn^{2+}] = 0.0024 M, [$\mathbf{L}^{17}$] = 0.003 M, pH (bottom up) = 2,30, 5,44, 5,7, 7,8, 8,73, 9,63, 10,66).

It is interesting to compare the pKs of coordinated water deprotonation in tren (pK = 9.17 (Cu), 10.4 (Zn)) and $\mathbf{L}^{17}$ (pK = 8.41 (Cu), 9.34 (Zn)) complexes. Although, several reasons may lead to the higher water acidity in the present systems, the conformationally less labile pyridine rings in Zn($\mathbf{L}^{17}$)(OH) (see above) may indicate H-bonding network between the hydroxide ion and pyridine nitrogen(s), which stabilize the position of the ring(s) and facilitate the formation of M–OH^- moiety.

2.8 Copper(II) complexes of a 5-pyrazolylmethyl substituted tren derivative: solution equilibrium, structure and catecholase activity (copper(II) complexes of $\mathbf{L}^{15}$ [8]).

As detailed in part ***2.6*** recently we developed a new tripodal ligand $\mathbf{L}^{10}$ [6], which forms highly stable mononuclear complex. Nevertheless it readily transforms into a unique trinuclear species that features a tetra(pyrazolate)-bridged linear tricopper(II) core (Figure 14). The triply deprotonated trinuclear complex ($Cu_3H_{-3}(\mathbf{L}^{10})_2$) is an efficient catechol oxidase mimic, which shows a surprisingly low pH optimum at pH = 5.6.

In order to explore the role of tripodal platforms in the stability, structure and enzyme mimicry, we designed the new tripodal ligand $\mathbf{L}^{15}$, a tren-based variant of tachpyz, and studied its copper(II) complexes both in solution and in solid phase. To screen the enzyme

mimetic properties of the copper(II)-$\mathbf{L}^{15}$ complexes, and to compare to those of $\mathbf{L}^{10}$ [6], we also investigated their catecholase activity by using 3,5-di-tert-butylcatechol (H_2dtbc) as model substrate.

The $[Cu(\mathbf{L}^{15})]^{2+}$ crystallized in the monoclinic $P2_1/c$ space group with the inclusion of two perchlorate anion (Figure 24). The two non-coordinated pyrazole nitrogens are involved in intramolecular hydrogen bonds with N-H protons of the neighbouring side chains which stabilize its position in the crystal structure. The position of the three side chaines is very different, the angles between the pyrazole ring planes are 53.5(2), 57.1(2) and 76.7(2). In the penta-coordinate structure four nitrogens are coordinating to the copper center in short distances (1.97-2.07 Å) and Cu1-N8 bond is slightly longer (2.15 Å). The geometry around the metal ion is in between a square pyramidal and trigonal bipyramidal ($\tau = 0.56$).

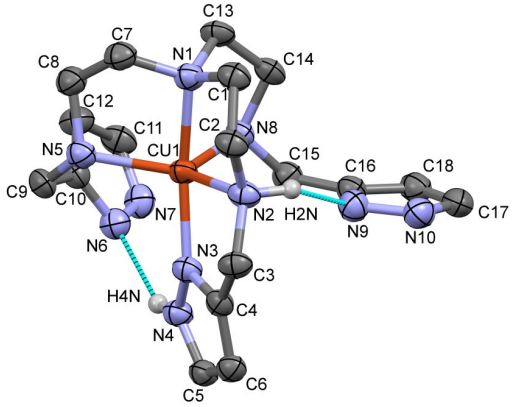

Figure 24. Molecular structure of the $[Cu(\mathbf{L}^{15})]^{2+}$ cation with atom numbering. Intramolecular hydrogen bonds are shown with blue lines, other hydrogens are omitted for clarity.

The complex formation in the copper(II)- $\mathbf{L}^{15}$ system was studied at M/L ratios of 1/2, 1/1, 3/2 and 2/1. At twofold metal ion excess precipitate formation was detected above pH 6, at other M/L ratios the solution was clear within the pH-range studied. Since in equimolar Cu(II)-$\mathbf{L}^{15}$ solution, the concentration of uncomplexed copper(II) at the beginning of pH-metric titration (pH ~ 1.8) was relatively low, pH-dependent Vis-near IR spectra were also collected between pH 0.7-11.2 in order to determine the correct formation constants. The combined evaluation of pH-potentiometric and UV-Vis spectrophotometric data indicated the formation of three mononuclear ($CuH\mathbf{L}^{15}$, $Cu\mathbf{L}^{15}$, $CuH_{-1}\mathbf{L}^{15}$) and three trinuclear ($Cu_3H_{-2}\mathbf{L}^{15}{}_2$, $Cu_3H_{-3}\mathbf{L}^{15}{}_2$ and $Cu_3H_{-4}\mathbf{L}^{15}{}_2$) complexes. The distribution curves of these complexes are depicted in Figure 25.

In equimolar solution the highly stable $CuH\mathbf{L}^{15}$ is the dominant species around pH 3. Its stability is considerably higher than that of the corresponding complex of $\mathbf{L}^{10}$, even considering the differences in the basicity of the ligands. This indicates the coordination of an additional donor group, i.e. the tertiary nitrogen in $CuH\mathbf{L}^{15}$. The two absorption bands observed on the Vis-near IR spectrum of $CuH\mathbf{L}$ at 626 nm ($\varepsilon = 135$ $M^{-1}cm^{-1}$) and 880 nm ($\varepsilon = 53$ $M^{-1}cm^{-1}$) clearly indicate square pyramidal geometry around the metal ion with relatively strong apical coordination. This conclusion is also supported by the EPR parameters of the species $CuH\mathbf{L}^{15}$ ($g_o = 2.105(1)$, $A_o = 64.7(5)$ G, $g_\perp = 2.053(2)$, $g_{//} = 2.236(2)$, $A_\perp = 19(1)$, $A_{//} = 170(1)$ G). The deprotonation of $CuH\mathbf{L}^{15}$ ($pK = 4.13$) results in the formation of $Cu\mathbf{L}^{15}$, a unique species between pH 6-8. During this deprotonation both the Vis-near IR and the low temperature EPR spectra (Figure 26) indicate fundamental changes in the coordination sphere of copper(II). Both the typical d-d transitions (an intense band at 790 nm with a high energy

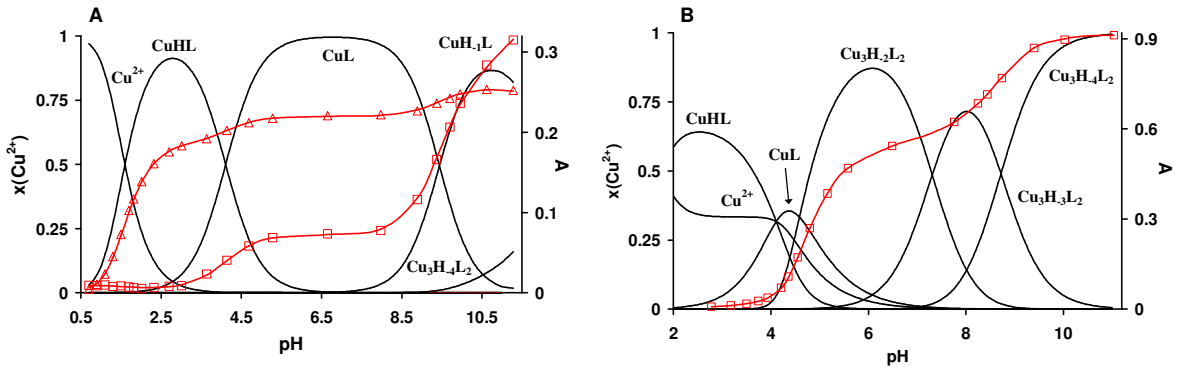

Figure 25. Speciation diagram of the copper(II)-$\mathbf{L}^{15}$ 1:1 (A) and 3:2 (B) systems, and the pH-dependent changes of absorbances at 420 nm (square) and 628 nm (triangle). T = 298 K, I = 0.1 M NaCl, [Cu^{2+}] = 0.001 M (A), 0.003 M (B).

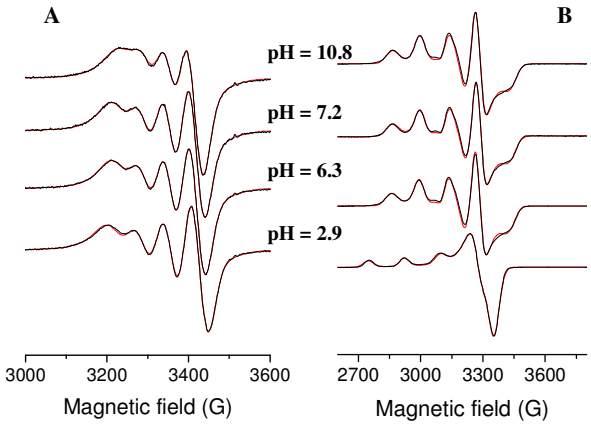

Figure 26. Experimental (red) and simulated (black) EPR spectra of the copper(II)-$\mathbf{L}^{15}$ 1/1 system at room temperature (A) and at 77 K (B).

shoulder at 640 nm), and the 'reversed' low temperature EPR spectra (g_o = 2.114(1), A_o = 59.4(5) G, $g_{x/y/z}$ = 2.195(2)/2.134(2)/2.010(1), $A_{x/y/z}$ = 134(2)/85(2)/-50(1) G) indicate distorted trigonal bipyramidal geometry around the metal ion, as seen in the crystal structure (Figure 24).

Considering that $\mathbf{L}^{15}$ offers seven nitrogens for the formation of fused chelate rings, its 5N coordination in a distorted trigonal bipyramidal geometry is surprising, especially, that this type of geometry has not been observed for the other potentially heptadentate tren derivatives. It seems that in the present case the strong coordinating ability of tren-like subunit is the governing factor, and the pyrazole rings occupy only the coordination position left free by the amino nitrogens.

In order to compare the metal ion binding abilities of tren and $\mathbf{L}^{15}$, we calculated the conditional stability constants at a given pH 7.4 ($K_{cond}(pH) = (\Sigma[MH_xL]/([M^{2+}]_{free} \times (\Sigma[H_xL]_{free}))$. The corresponding log K_{cond}(pH = 7.4) values are 12.6, 17.1, respectively. The more than 4 orders of magnitude higher conditional stability constant of Cu**L** compared to Cu(tren) confirms the additional coordination of a pyrazole ring.

Above pH 8 the potentiometric data indicated further deprotonations and the formation of $CuH_{-1}\mathbf{L}^{15}$. Both the Vis-near IR and EPR spectra (Figure 26) indicate some slight differences between Cu$\mathbf{L}^{15}$ and $CuH_{-1}\mathbf{L}^{15}$ (d-d bands at 756 nm, more intense shoulder at 640

nm, g_o = 2.111(1), A_o = 52.8(5) G, $g_{x/y/z}$ = 2.194(2)/2.132(2)/2.010(1), $A_{x/y/z}$ = 134(2)/82(2)/-54(1) G), but the typical features of trigonal bipyramidal geometry are retained. The p*K* of this deprotonation (9.56) is only slightly higher than that of Cu(tren) (pK = 9.17, Table 4), in which the proton loss of a water molecule bound in the fifth coordination position takes place. Considering that in $CuH_{-1}\mathbf{L}^{15}$ the fifth coordination position is occupied, and that similar process is absent for the Cu($\mathbf{L}^{16}$) complex up to pH 11, the observed deprotonation is most probably related to the copper-bound pyrazole ring. Indeed, the deprotonation results in the development of a CT band around 420 nm with medium intensity (Figure 25.A), which is very similar to the $N_{pyr}^{-}\rightarrow$Cu(II) CT transition reported earlier for some copper(II) complex.

The presence of mono-coordinated pyrazolate ring creates the possibility for the formation of oligonuclear complexes, which was indeed observed above pH 10 even in equimolar solutions. At 3/2 Cu(II)/$\mathbf{L}^{15}$ ratio, their formation is more pronounced and three trinuclear complexes can be identified (Figure 25.B). The presence of trinuclear complexes was also confirmed by Maldi-TOF MS. Around pH 6 the doubly deprotonated $Cu_3H_{-2}\mathbf{L}^{15}_2$ complex is dominant, and its stepwise deprotonations (p*K* = 7.56, 8.62) result in the formation of $Cu_3H_{-4}\mathbf{L}^{15}_2$, a unique species above pH 10 (Figure 25.B). Above pH 4, parallel with the formation of trinuclear complexes, the color of the solution shows gradual changes from blue to green than to brownish, due to the development of intense charge transfer (CT) band around 420 nm (Figures 25.B). Considering the structure of $\mathbf{L}^{15}$, the formation of such intense CT bands are consistent only with copper(II) promoted deprotonations of pyrazole rings, *i.e.* the formation of pyrazolate-bridged trinuclear core in $Cu_3H_{-x}\mathbf{L}^{15}_2$ (x = 2,3,4). Similar observations were made in the Cu(II)-$\mathbf{L}^{10}$ system, too, therefore the structure of $Cu_3H_{-4}\mathbf{L}^{15}_2$ should be analogous to the crystallographically characterized $[Cu_3H_{-4}(\mathbf{L}^{10})_2](ClO_4)_2\times 5H_2O$ (see Figure 14 [6]).

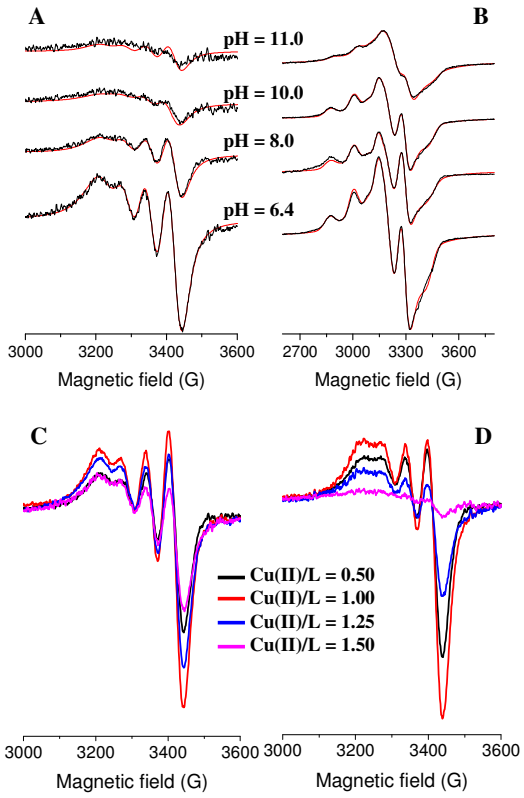

Figure 27. Experimental (red) and simulated (black) EPR spectra of the copper(II)-$\mathbf{L}^{15}$ 3/2 system at room temperature (A) and at 77 K (B), and the comparison of EPR intensities at pH 6.4 (C) and 10 (D) with increasing Cu(II)/$\mathbf{L}^{15}$ ratios.

The species $Cu_3H_{-2}\mathbf{L}^{15}_2$ formed around pH 6 has well resolved EPR spectra both at 298 K and 77 K, and the EPR signal intensity gradually decreases with increasing pH, which is more pronounced at room temperature (Figure 27.A and B). On the other hand, the EPR intensity passes through a maximum with increasing Cu(II)/$\mathbf{L}^{15}$ ratios (at constant concentration of $\mathbf{L}^{15}$), and the maximum is observed at 1/1 Cu(II)/$\mathbf{L}^{15}$ ratio (Figure 27.C and D). At pH 6.4 the intensities observed at 0.5 and 1.5 Cu(II)/$\mathbf{L}^{15}$ ratios are nearly identical (Figure 26.C). *i.e.* at 1.5 Cu(II)/$\mathbf{L}^{15}$ ratio only 1/3 of the expected intensity can be observed. All these facts are in excellent agreement with a coupled tricopper(II) core with total spin of S = ½. This implies that the central copper(II) is antiferromagnetically coupled with one of the two peripheral copper(II) ions. At pH 10 (Figure 27.D), the increasing Cu(II)/$\mathbf{L}^{15}$ ratios results in considerably loss of EPR intensity (broadened spectra). In principle such broadening might be due to intramolecular exchange phenomena, which is more faster in the complexes with 3/4 pyrazolato bridges between the copper(II) centres. It is worth pointing out that the low temperature EPR spectra of the trinuclear complexes (Figure 27.B) clearly indicate, that the periferal copper(II) centres of the trinuclear complexes have trigonal bypiramidal geometry.

Although, in the Cu(II)-$\mathbf{L}^{10}$ and Cu(II)-$\mathbf{L}^{15}$ 3/2 systems similar trinuclear complexes are formed, the variation of the trigonal platforms results in fundamental differences concerning their relative stability. Due to the higher number of available donor atoms of $\mathbf{L}^{15}$ four 'free' pyrazole rings are available in $Cu_3H_{-2}\mathbf{L}^{15}_2$, which in turn are able to significantly stabilize the two-fold deprotonated trinuclear complex as compared to $Cu_3H_{-2}\mathbf{L}^{10}_2$ (Figure 28).

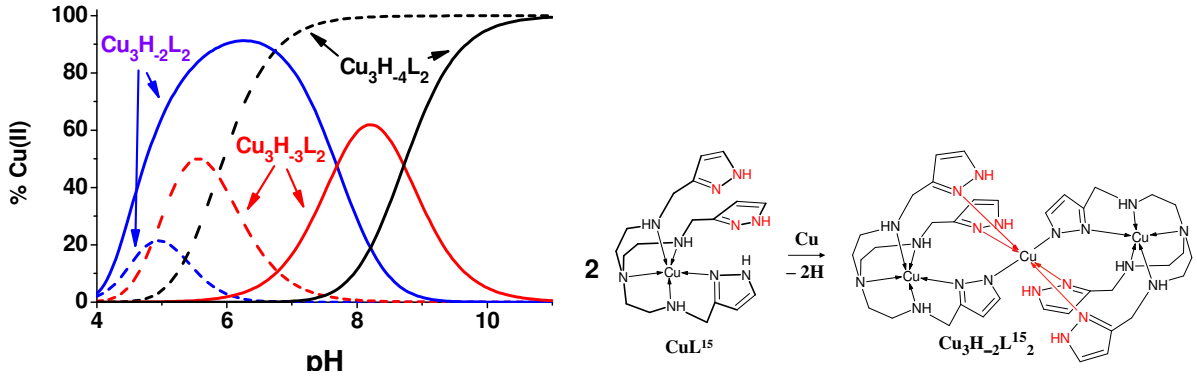

Figure 28. Speciation of the trinuclear complexes in the Cu(II)-$\mathbf{L}^{10}$ (dashed lines) and in the Cu(II)- $\mathbf{L}^{15}$ (solid lines) systems, and the schematic structure of $Cu_3H_{-2}\mathbf{L}^{15}_2$, with the pyrazole nitrogens available for the extra stabilization in red.

Due to the mentioned important stabilization provided by the four 'free' pyrazole rings, the speciation of the trinuclear complexes of $\mathbf{L}^{15}$ is rather different from that of $\mathbf{L}^{10}$, *i.e.* the formation of the three- and four-fold deprotonated trinuclear complexes is shifted by more than two pH units to the higher pH.

Using $\mathbf{L}^{15}$, our intention was to develop oxidative catalysts able to activate dioxygen, similarly to the copper(II) complexes of $\mathbf{L}^{10}$ (see part 2.6 and [6]). To this end we studied the catecholase activity of the Cu(II)-$\mathbf{L}^{15}$ complexes using di-*tert*-butyl-catechole as substrate, and compared to that of the Cu(II)-$\mathbf{L}^{15}$ system.

In both cases, the triply deprotonated trinuclear complexes were proved to be the catalytically active species. Since the additional binding site in $\mathbf{L}^{15}$ stabilizes the two-fold deprotonated species, the observed pH – rate constant profiles are considerably different in the two cases (Figure 29). The $Cu_3H_{-2}\mathbf{L}^{10}_2$ complex showed surprisingly low pH optimum of the catalytic reaction at pH 5.6 [6]. In the present case, the The $Cu_3H_{-2}\mathbf{L}^{15}_2$ species has a

maximum activity at two units higher pH. This implies, that the dtbc oxidation can be easily controlled by the coordination environment of the central metal ion.

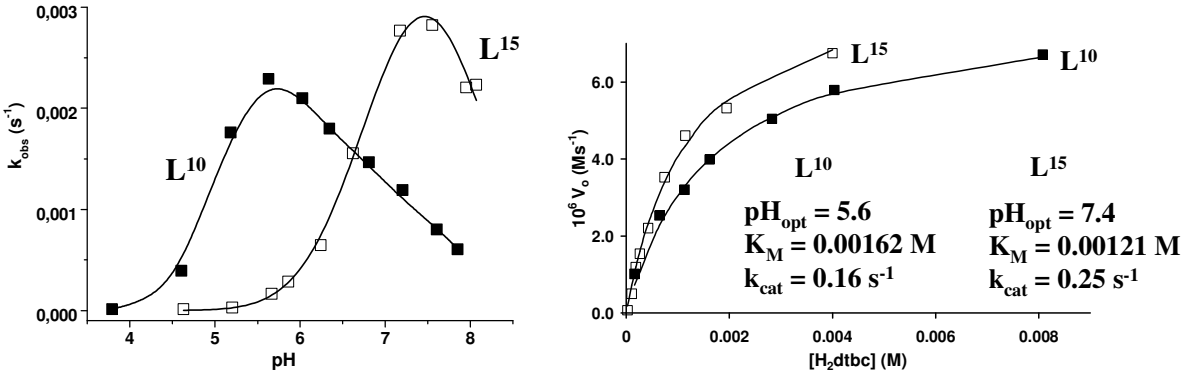

Figure 29. Kinetic data of the oxidation of dtbc in 50 w% ethanol-water promoted by the copper(II)-$\mathbf{L^{10}}$ (filled square) and Cu(II)-$\mathbf{L^{15}}$ (open square) 3:2 systems. Left: pH–rate constant profile (T = 298 K, $[Cu^{2+}]/3$ = 0.05 mM, $[dtbc]_0$ = 1.8 mM). Right: V_0 of dtbc oxidation as a function of dtbc concentration catalyzed by the copper(II)-$\mathbf{L^{10}}$ (filled square, pH=5.6) and Cu(II)-$\mathbf{L^{15}}$ (open square, pH= 7.4) 3:2 systems.

Nevertheless, at the optimal pH both systems show high and nearly identical catecholase activity (Figure 29). It is worth to mention that the fully deprotonated trinuclear complexes are inactive, since the substrate is no longer able to coordinate to the trinuclear core. Moreover, the mononuclear complex, having identical structure than the terminal copper(II) ions is also inactive. Therefore, we assume that the central copper(II) ion, with unsaturated and pyrazolate-bound coordination sphere, has fundamental role in binding and oxidation of catechols.

Our work pointed out that by derivatization of some simple tripodal platforms (tren, tach) it is possible to fine-tune the coordination chemical properties such as structure and stability, but also some important enzyme like features, such as activity and its pH-profile, and even a new binding site for the catalytic metal ion can be created under allosteric controll.

2.9 Transition metal complexes of $\mathbf{L^{13}}$ and $\mathbf{L^{18}}$ [9]

$\mathbf{L^{13}}$ forms highly stable 5N coordinated ML complexes with manganese(II), copper(II) and zinc(II) (Table 1). The complex $\mathbf{Cu}L^{13}$ is a unique species between pH 5-8 (Figure 30). Its formation constants is several orders of magnitudes higher than the corresponding Cu(tach) species, implying the additional coordination of the pyridine ring. Indeed, according to our X-ray and spectroscopic data $\mathbf{CuL^{13}}$ is 4N coordinated, and has strongly distorted geometry (τ = 0.49) in between the square pyramidal and trigonal bipyramidal structures (Figure 30).

Table 1. Logarithmic formation constants of the metal complexes of $\mathbf{L^{13}}$ and tach (T = 298 K, I=0.1M (NaCl), with estimated errors in parentheses (last digit)).

	log β			
	Mn	Zn	Cu	Cu(tach)
MH_2L	---	---	23.68(2)	---
MHL	---	---	---	15.95
ML	4.67(8)	9.74(3)	15.54(1)	10.86
$MH_{-1}L$	---	-0.33(4)	6.18(1)	2.36
$MH_{-2}L$	-12.3(6)	---	---	---

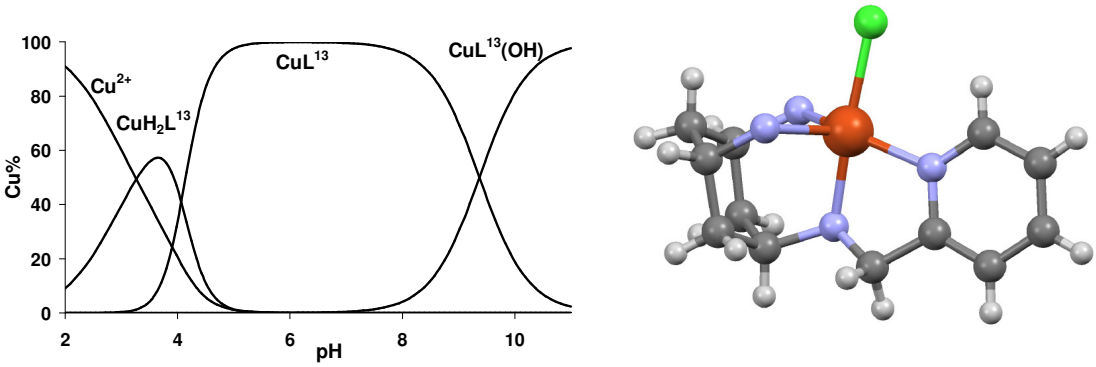

Figure 30. Left: Speciation diagram of the copper(II)-$\mathbf{L}^{13}$ system (T = 298 K, I = 0.1 M NaCl, $[Cu^{2+}]$ = 0.001), and the crystal structure of $[Cu\mathbf{L}^{13}(Cl)]\times(ClO_4)$ on the right.

Above pH 9-10 the formation of mixed hydroxo complexes was observed in all cases. Both $Zn\mathbf{L}^{13}$ and $Zn\mathbf{L}^{13}(OH)$ have slow ligand exchange on the NMR time-scale (Figure 31). The important differences in the spin coupling pattern between the free and bound ligand indicate, in this case, too, the switch between the two chair conformations (triequatorial NH → triaxial NH). The chemical inequivalence of benzylic protons (~ 4.2 ppm) shows

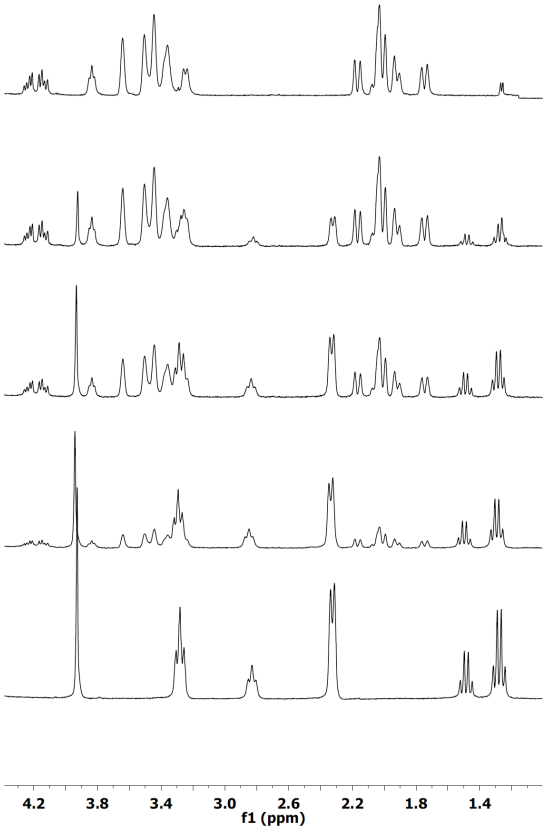

Figure 31. ^{1}H NMR spectra of $\mathbf{L}^{13}$ with increasing concentrations of zinc(II) (pH = 7.2, from bottom to top $Zn/\mathbf{L}^{13}$ = 0, 0.25, 0.5, 0.75, 1.0)

conformational rigidity even within the 2-pyridylmethyl arms, suggesting 4N coordination of the ligand. Interestingly, the ABX quartet of the benzylic protons are coupled with the adjacent secondary NH proton, which itself also appear on the spectrum around 3.8 ppm. The

deceleration of the proton exchange with the bulk water is due to the coordination of the secondary nitrogen to zinc(II).

L^{18} forms highly stable 5N coordinated monocomplexes with all investigated metal ions. For the less stable Fe(II)- and Mn(II)-complexes extra deprotonation was observed above pH 9 (Table 2), resulting in the formation of mixed hydroxo-complexes. Our spectroscopic data (Figure 32) indicate octahedral geometry for CuH**L**^{18}, and trigonal bipyramidal structure for Cu**L**^{18}. The UV-Vis and ^{1}H NMR experiments suggest that the Fe^{II}**L**^{18} is an octahedral low spin complex.

Table 2. Logarithmic formation constants of the metal complexes of **L**^{18} and tach (T = 298 K, I=0.1M (NaCl), with estimated errors in parentheses (last digit)).

	log β				
	Cu(II)	Zn(II)	Co(II)	Fe(II)	Mn(II)
MHL	25.85(1)	19.83(5)	19.72(2)	16.85(4)	14.2(1)
ML	22.19(1)	15.55(1)	14.02(2)	10.04(4)	7.10(3)
MH$_{-1}$L	—	—	—	0.10(5)	-3.77(4)

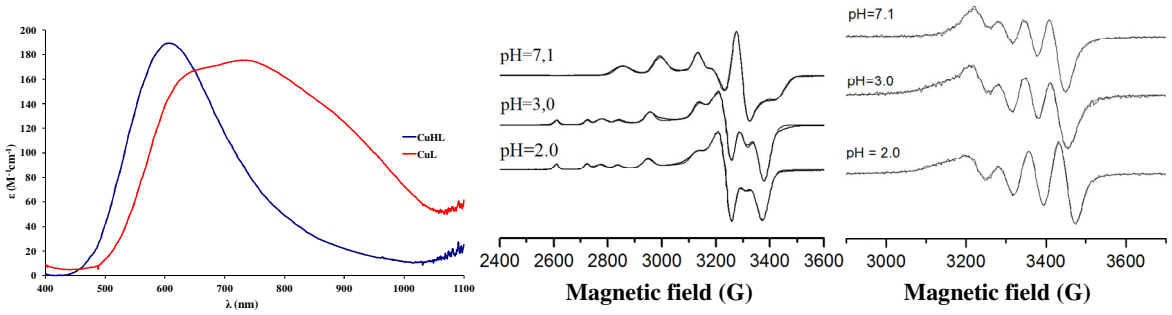

Figure 32. Individual molar visible spectra of CuH**L**^{18} and Cu**L**^{18} (left) and EPR spectra of the Cu(II)-**L**^{18} 1/1 system both at 77 and 298 K.

The Zn**L**^{18} complex has slow ligand exchange on the NMR time-scale (Figure 34). All methylene protons, including the benzylic protons, are inequivalent due to the formation of fused chelate rings, which confirm the 5N coordination of the ligand.

In the Co(II)-**L**^{18} system, above pH 8 an irreversible oxidation of the metal ion takes place even under strong bubbling of argon gas. Since until this pH the the equilibrium system is reversible, our potentiometric data were evaluated only up to pH 7.5. It is interesting to compare the important difference in the speciation of CoH**L**^{18} and ZnH**L**^{18} (Figure 34), which is surprising taking into account their nearly identical formation constants (Table 2). The reason of this difference is the relatively important difference in the stability of Co**L**^{18}/Zn**L**^{18} (log $\beta_{ZnL^{18}}$ = 15.55, log $\beta_{CoL^{18}}$ = 14.12, Table 2), which is probably due to the different preference of the two metal ions for the trigonal bipyramidal geometry. In the case of the d10 zinc(II) ion there is no clear geometrical preference, but due to the crystal field stabilisation energy, the octahedral geometry is preferred for Co(II).

Finally, both Cu**L**^{13} and Cu**L**^{18} show catalase-like activity, but this property is currently still under investigation.

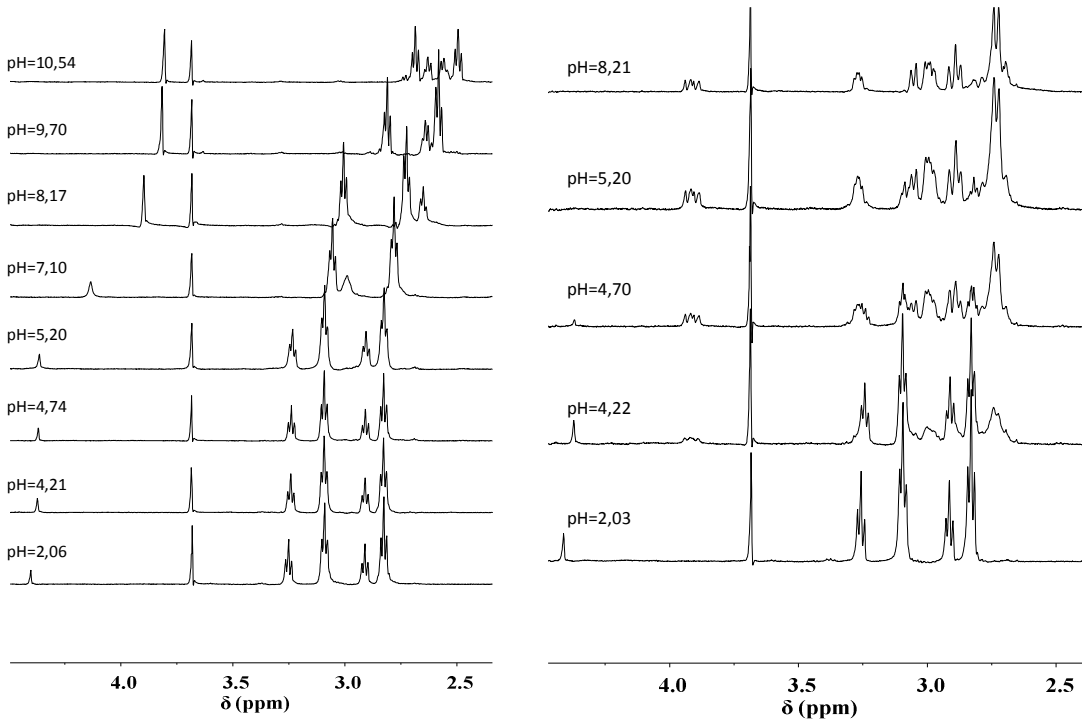

Figure 33. pH dependent ^{1}H NMR spectra of the free ligand $\mathbf{L}^{18}$ (left) and Zn(II)-$\mathbf{L}^{18}$ 1/1 system (right). The singlet at 3.7 ppm is the signal of the internal reference dioxane.

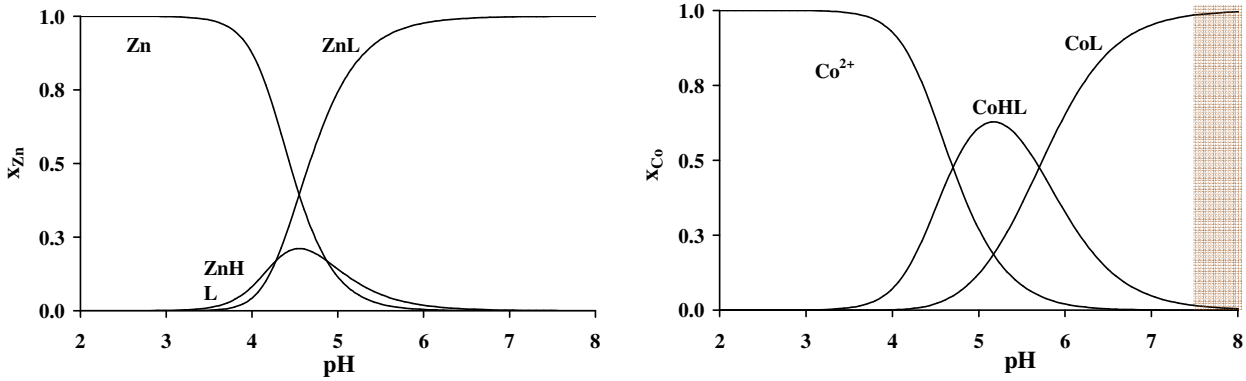

Figure 34. Speciation diagram of the zinc(II)-$\mathbf{L}^{18}$ (left) and cobalt(II)-$\mathbf{L}^{18}$ (right) 1/1 systems (T = 298 K, I = 0.1 M NaCl, [M^{2+}] = 0.001)

References

[1] D. Árus, N. V. Nagy, Á. Dancs, A. Jancsó, R. Berkecz and T. Gajda, 'A minimalist chemical model of matrix metalloproteinases - can small peptides mimic the more rigid metal binding sites of proteins?', *J. Inorg. Biochem.*, 2013, **126**, 61–69.

[2] Árus, D.; Dancs, Á.; Nagy, N.V.; Gajda, T., 'A comparative study on the possible zinc binding sites of the human ZnT3 zinc transporter protein', *Dalton Trans.*, 2013, **42**, 12031-12040.

[3] Á. Dancs, N. May, K. Selmeczi, Zs. Darula, A. Szorcsik, F. Matyuska, T. Páli, T. Gajda, 'Tuning the coordination properties of multi-histidine peptides by using a tripodal scaffold: solution chemical study and catechol oxidase mimicking', *New J. Chem.*, 2017,**41**, 808-823.

[4] Á. Dancs, N. May, K. Selmeczi, T. Gajda, 'Modulating the coordination chemistry of the tripodal platform tris(2-aminoethyl)amine (tren) by gradual N-substitution with L-histidyl units', under preparation to be submitted in april 2017.
[5] T.A. Lönnberg, M. Helkearo, A. Jancsó, T. Gajda, 'Mimics of small ribozymes utilizing a supramolecular scaffold', *Dalton Trans*., 2012, **41**, 3328-3338.
[6] A. Szorcsik, F. Matyuska, A. Bényei, N.V. Nagy, R.K. Szilágyi, T. Gajda, 'A novel 1,3,5-triaminocyclohexane-based tripodal ligand forms a unique tetra(pyrazolate)-bridged tricopper(II) core: solution equilibrium, structure and catecholase activity', *Dalton Trans*., 2016, **45**, 14998-15012.
[7] F. Matyuska, A. Szorcsik, N.V. May, Á. Dancs, É. Kováts, A. Bényei, T. Gajda, 'Tailoring the local environment around metal ions: solution chemical and structural study of some multidentate tripodal ligands', submitted to Dalton Trans. In 11.01.2017 (DT-ART-01-2017-000104)
[8] F. Matyuska, A. Szorcsik, N.V. May, Á. Dancs, A. Bényei, T. Gajda, 'Copper(II) complexes of a 5-pyrazolylmethyl substituted tren derivative: solution equilibrium, structure and catecholase activity', under preparation, to be submitted in may 2017.
[9] work in progress, to be submitted in june 2017.